Microbeam X-ray Absorption Near-edge Spectroscopy of Alloying Elements in the Oxide Layers of Irradiated Zircaloy-2

Aditya P. Shivprasad[1], Arthur T. Motta[1], Aylin Kucuk[2], Suresh Yagnik[2], and Zhonghou Cai[3]

ABSTRACT

Hydrogen pick-up of zirconium-based fuel cladding and structural materials during in-reactor corrosion can degrade fuel component, as the ingress of hydrogen can lead to the formation of brittle hydrides. In the BWR environment, Zircaloy-2 fuel cladding and structural components such as water rods and channels can experience accelerated hydrogen pick-up, while Zircaloy-4 components exposed to similar conditions do not. Because the principal difference between the two alloys is that Zircaloy-2 contains nickel, accelerated hydrogen pick-up has been hypothesized to result from the presence of nickel. However, an understanding of the mechanism by which this acceleration occurs is still lacking. This research investigates the link between hydrogen pick-up and the oxidation behavior of alloying elements when incorporated into the oxide layers formed on zirconium alloys when corroded in-reactor. In this study, synchrotron radiation microbeam X-ray absorption near edge spectroscopy (XANES) at the Advanced Photon Source was performed on carefully selected BWR-corroded Zircaloy-2 water rods at assembly-averaged burn-up ranging from 32.8 to 74.6 GWd/MTU to determine the oxidation states of alloying elements, such as iron and nickel, within the oxide layers, as a function of distance from the oxide-metal interface at high burn-up. Samples were chosen for comparison based on having similar oxide thicknesses,

[1] Dept. of Mechanical and Nuclear Engineering, The Pennsylvania State University, University Park, PA, 16802, United States of America
[2] Electric Power Research Institute, Palo Alto, CA, 94304, United States of America
[3] Advanced Photon Source, Argonne National Laboratory, Argonne, IL, 60439, United States of America

processing, elevation, reactors, and fluences, but different hydrogen pick-up fractions. Examinations of the oxide layers formed on these samples showed that: (i) the oxidation states of these alloying elements changes with distance from the oxide metal interface, (ii) these elements exhibit delayed oxidation relative to the host zirconium and, (iii) nickel in Zircaloy-2 remained metallic in the oxide layer at a longer distance from the oxide/metal interface than iron. Analysis of these results showed an apparent correlation between the delayed oxidation of nickel and higher hydrogen pick-up of Zircaloy-2 at high burn-up.

Keywords

Zircaloy-2, hydrogen pick-up, XANES, alloying elements, high burn-up, oxidation state

Introduction

During the initial development of nuclear fuel cladding for light water reactors, the large variance in mechanical behavior seen in notched-bar impact testing of both out-of-pile and in-reactor-corroded Zircaloy-2 was attributed to a hydride phase that formed due to high hydrogen pickup [1-2]. Detailed corrosion testing of zirconium alloy coupons of various compositions showed that alloys with higher nickel content absorbed larger quantities of hydrogen. The removal of nickel, altogether, significantly reduced the percentage of hydrogen absorbed relative to the amount produced during the corrosion reaction, called the hydrogen pick-up fraction (HPUF) [3-6]. The subsequent removal of nickel from Zircaloy-2 and optimization of alloying-element contents resulted in the development of Zircaloy-4. However, because Zircaloy-2 exhibited better corrosion resistance in steam environments, it became the industry standard for the Boiling Water Reactor (BWR) fuel cladding [2, 7-8]. Although the hydrogen pick-up properties of Zircaloy-2

have been studied since its development, the role of nickel in promoting hydrogen pick-up is not well understood.

HPUF has been used in the past as a measure of the tendency of a material to absorb hydrogen. It should be noted, however, that due to complex phenomena involved, HPUF is not an inherent physical property of the material, per se, but is the result of the interaction of material properties with the corrosion environment. Also, because HPUF depends directly on the oxide layer thickness, a higher HPUF does not necessarily mean higher hydrogen content.

Early studies performed by Yeniscavich [3] tested nickel-, copper-, and iron-enriched Zircaloy-2 samples under reactor conditions. Results showed that increasing nickel caused a significant increase in hydrogen absorption, while copper and iron had little effect on the hydrogen absorption properties. Additionally, hydrogen pick-up was noted to increase under irradiation [3]. From these experiments, the authors concluded that nickel acted as a catalyst for surface reactions that allowed hydrogen to enter the oxide layer. However, because weight gains for these samples were not recorded, the hydrogen pick-up fractions of the tested samples could not be compared with those of other experiments.

Recent results have indicated that Zircaloy-2 cladding exhibited increased HPUF at high burn-up in BWR [9]. This change in hydrogen pick-up behavior was attributed to the dissolution of the finely distributed second-phase particles (SPPs) under irradiation [7, 9]. More recent examinations of Zircaloy-2 structural components corroded in commercial BWRs showed that above 50 GWd/MTU burn-up, hydrogen pick-up exhibited wide variability [7, 10]. This change in hydrogen pick-up behavior at high burn-up was only observed in Zircaloy-2 components and not in Zircaloy-4. **FIG. 1** shows the hydrogen pick-up fraction for Zircaloy-2 and Zircaloy-4

components in Boiling Water Reactors. It is clear that, at high burn-up, Zircaloy-2 components show a wide range of HPUF, while the HPUF of Zircaloy-4 remains low. These results suggest that nickel may play an important role in this change in hydrogen pick-up fraction.

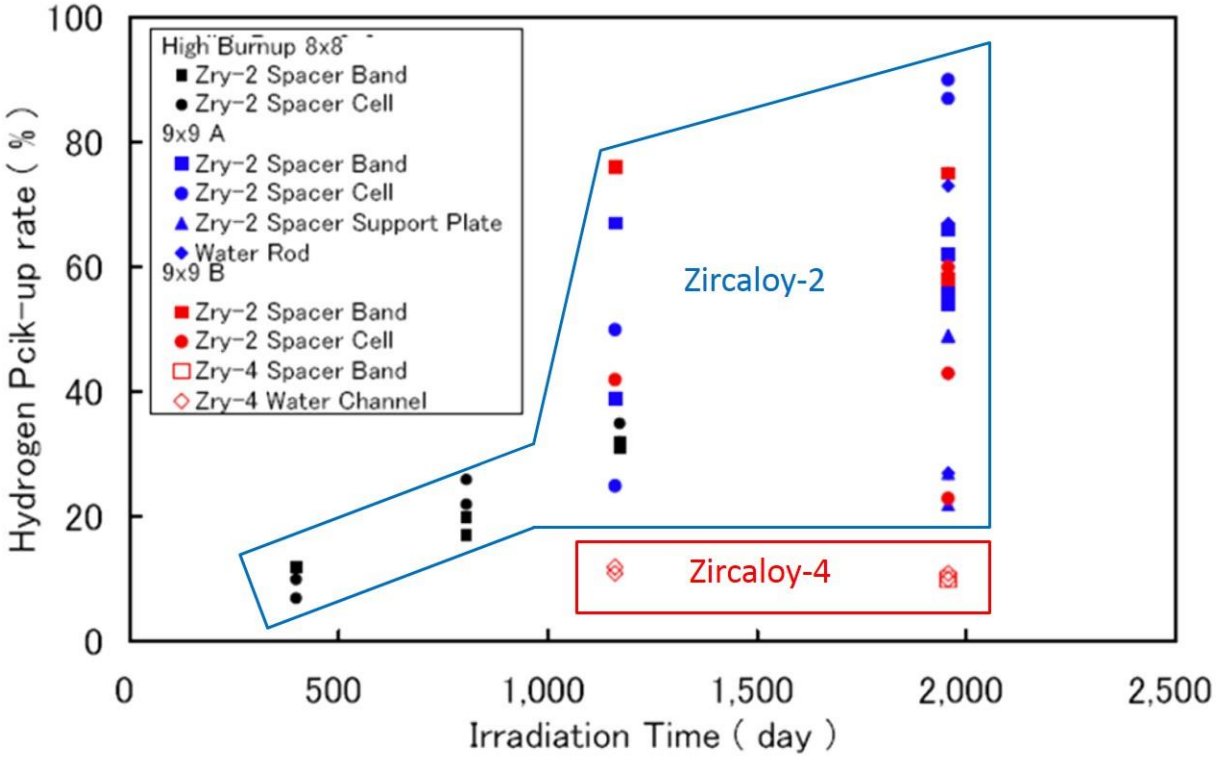

FIG. 1 Hydrogen pick-up fraction of Zircaloy-2 and Zircaloy-4 components at high burn-up in the BWR environment. Figure modified from [10].

To discern the role of nickel in the hydrogen pickup process during irradiation, one property of particular interest is the oxidation state of nickel atoms upon their incorporation into the advancing oxide layer. Previous work has shown that iron and chromium are indeed noble with respect to zirconium and thus remain metallic in Zircaloy-4 oxide layers formed in high-temperature-autoclave environments [11-14]. To obtain information on the oxidation state of iron and nickel in a spatially resolved manner (i.e., as a function of distance from the interface),

microbeam X-ray absorption near-edge spectroscopy (XANES) was used [11-12, 15]. With this technique (performed at the Advanced Photon Source (APS) at Argonne National Laboratory) a microfocused X-ray beam was used to probe the oxide layer at the submicron level. Using cross-sectional samples of in-reactor corroded material allowed for examinations as functions of distance from the oxide/metal interface.

Experimental Methods

MATERIALS

For this study, a focused set of samples was chosen to highlight the differences that lead to high hydrogen pick-up of Zircaloy-2 in BWRs. To isolate the effect of heat flux, the samples were taken from water rods (WR) exposed to high fluence so that corrosion occurred under irradiation but in the absence of heat flux, except for the relatively small contribution from gamma heating. Detailed descriptions of these irradiated samples are given in **TABLE 1** and images of the water rod samples are shown in **FIG. 2**. Additionally, mean precipitate size and density for each sample are given in **TABLE 2**, as measured by Nippon Nuclear Fuel Development Co., Ltd (NFD).

All materials were composed of Zircaloy-2 and have undergone several alpha anneal heat treatments, which consisted of a vacuum anneal at 577 °C after the beta quench, prior to irradiation. Cumulative annealing parameters (CAP) for the different samples are shown in **TABLE 1** and were calculated using a Q/R value of 40,000. Compositions given in **TABLE 1** refer to nominal compositions at fabrication. The water-chemistry history, given in the second row of **TABLE 1**, distinguishes between hydrogen water chemistry (HWC), the presence of zinc and noble metal (NM) additions to the coolant. The surface temperature for all samples during exposure was approximately 288 °C, which is the saturation temperature in a BWR.

The samples in **TABLE 1** are divided into two main sets. The first set compares two materials with similar oxide thicknesses but widely different hydrogen pickup fractions and were both corroded in the Limerick-1 reactor. Both water rods were manufactured during the same production period and were irradiated in the core in symmetric locations for three 24-month cycles. The bundle from which Material 10 was taken was discharged, while the bundle from which Material 13 was taken was irradiated for one more cycle (24 months). While the average outer oxide thicknesses of Material 10 (low HPUF) and Material 13 (high HPUF) were 23 μm and 27 μm, respectively, Material 10 had a HPUF of 15% and Material 13 had a HPUF of 51%. From the as-irradiated precipitate size and density measurements given in **TABLE 2**, no significant difference in Laves phase precipitate size and density was observed between Materials 10 and 13, post-irradiation. However, the size and density of nickel-containing precipitates in Material 13 was significantly smaller than in Material 10. However, because these values were measured using transmission electron microscopy (TEM), it is not known whether these differences are real or a result of measurement variability.

In the second set of samples, two materials are again compared. These samples were taken from water rods corroded in the Dresden-2 reactor. Material 17 (low HPUF, 28%) exhibited an outer oxide thickness of approximately 3.5 μm and Material 21 (high HPUF, 69%), an outer oxide thickness of approximately 16 μm. Like the previous set of samples, these water rods were irradiated in symmetric fuel assemblies for three 24-month cycles. The assembly containing Material 17 was discharged after these three cycles, while the assembly containing Material 21 remained for an additional 24-month cycle. Comparing as-irradiated precipitate sizes and densities for Materials 17 and 21 from **TABLE 2** shows no significant difference in size or density for Laves phase precipitates and nickel-containing precipitates. Comparison of precipitate size and density

between the first (Materials 10 and 13) and second (Materials 17 and 21) pairs showed that Materials 17 and 21 exhibited larger Laves phase precipitates, but at a lower density. In contrast, the nickel-containing precipitates of Materials 17 and 21 were of a similar size as Materials 10 and 13, but at a much lower density. Because the first set of samples underwent a different heat treatment than the second set, initial precipitate size and distribution were different, so a comparison of as-irradiated precipitate sizes was not straightforward.

A fifth sample, called Archive 1, was taken from the bottom of the same water rod as Materials 10. Although the neutron fluence at low elevations cannot be calculated precisely, it is assumed to be approximately 2×10^{21} n/cm^2 (E > 1 MeV). The sample is expected to have some irradiation damage, but because the fluence is low compared to that of the other samples located at higher elevations, damage should be substantially less. Therefore, the sample is assumed to be an indicator of thermal treatment effects only. Precipitate sizes and densities for Archive 1 are comparable to those of Materials 10 and 13, with the difference that the densities of both types of precipitates are higher for Archive 1 than Materials 10 and 13. This is consistent with assumption that Archive 1 received a lower fluence than the other samples and measurements in this sample were indicators of heat treatments effects only.

Oxide thicknesses for all samples, except for Archive 1, were measured using metallography at GEH Vallecitos Hot Cell Facility and oxide thickness measurements using microbeam synchrotron radiation in this study were consistent with metallographic examinations to approximately five micrometers. The oxide layers formed on the Zircaloy-2 materials in this study generally formed black, shiny oxide layers. The oxide layers are generally uniform, but display more variation than oxide layers formed on Zircaloy-4. Although Material 17 exhibits what appears to be spots of nodular corrosion and Material 10 exhibits a lighter colored oxide, the oxide layers are protective

and not spalling, so that the weight gain and hydrogen pick-up can be compared to that of the other samples in this study.

Hydrogen contents of all samples, except for Archive 1, were measured with a LECO RH-2 hydrogen analyzer, which uses an inert gas fusion method to release hydrogen. In this apparatus, the sample was melted in a graphite crucible containing a tin flux. The evolved hydrogen was swept from the crucible with high-purity nitrogen gas to a thermal conductivity detector, where the change in thermal conductivity of the gas stream was measured and related to the hydrogen content through a series of calibration standards.

TABLE 1 Detailed descriptions of irradiated water rod (WR) materials analyzed in this study. Reported oxide thicknesses are average values. Initial examinations were performed at GEH Vallecitos Hot Cell Facility.

Material	Archive 1	Material 10	Material 13	Material 17	Material 21
Water chemistry history	HWC/Zinc/NM	HWC/Zinc/NM	HWC/Zinc/NM	HWC	HWC
Material type	Zry-2 WR	Zry-2 WR	Zry-2 WR	Zry-2 WR	Zry-2 WR
Composition at fabrication	Zr-1.29Sn-0.18Fe-0.10Cr-0.07Ni			Zr-1.55Sn-0.18Fe-0.12Cr-0.05Ni	
Cumulative Annealing Parameter (CAP) (h)	2.19×10^{-19}	2.19×10^{-19}	2.19×10^{-19}	N/A	N/A
Fluence (E > 1 MeV) at sample elevation (10^{21} n/cm^2)	~2	9.7	13.1	7.1	9.4
Inner oxide thickness (μm)	N/A	22	29	3.0	9
Outer oxide thickness (μm)	3.4	23	27	3.5	16
H content (wt. ppm)	N/A	250	1033	67	622
HPUF (%)	N/A	15	51	28	69
Exposure time (d)	2036	2036	2703	1665	2193
Bundle-average burn-up (GWd/MTU)	59.7	59.7	74.6	32.8	43.7

TABLE 2 Mean precipitate size and density for chromium- and nickel-rich precipitates. Values courtesy of NFD.

$Zr(Fe,Cr)_2$ precipitates					
	Archive 1	Material 10	Material 13	Material 17	Material 21
Mean SPP diameter (nm)	56	52	59	81	73
Density (m^{-3})	1.78×10^{19}	1.64×10^{19}	1.60×10^{19}	1.27×10^{19}	1.19×10^{19}

$Zr_2(Fe,Ni)$ precipitates					
	Archive 1	Material 10	Material 13	Material 17	Material 21
Mean SPP diameter (nm)	82	98	65	80	84
Density (m^{-3})	3.99×10^{18}	3.06×10^{18}	1.40×10^{18}	6.48×10^{17}	6.87×10^{17}

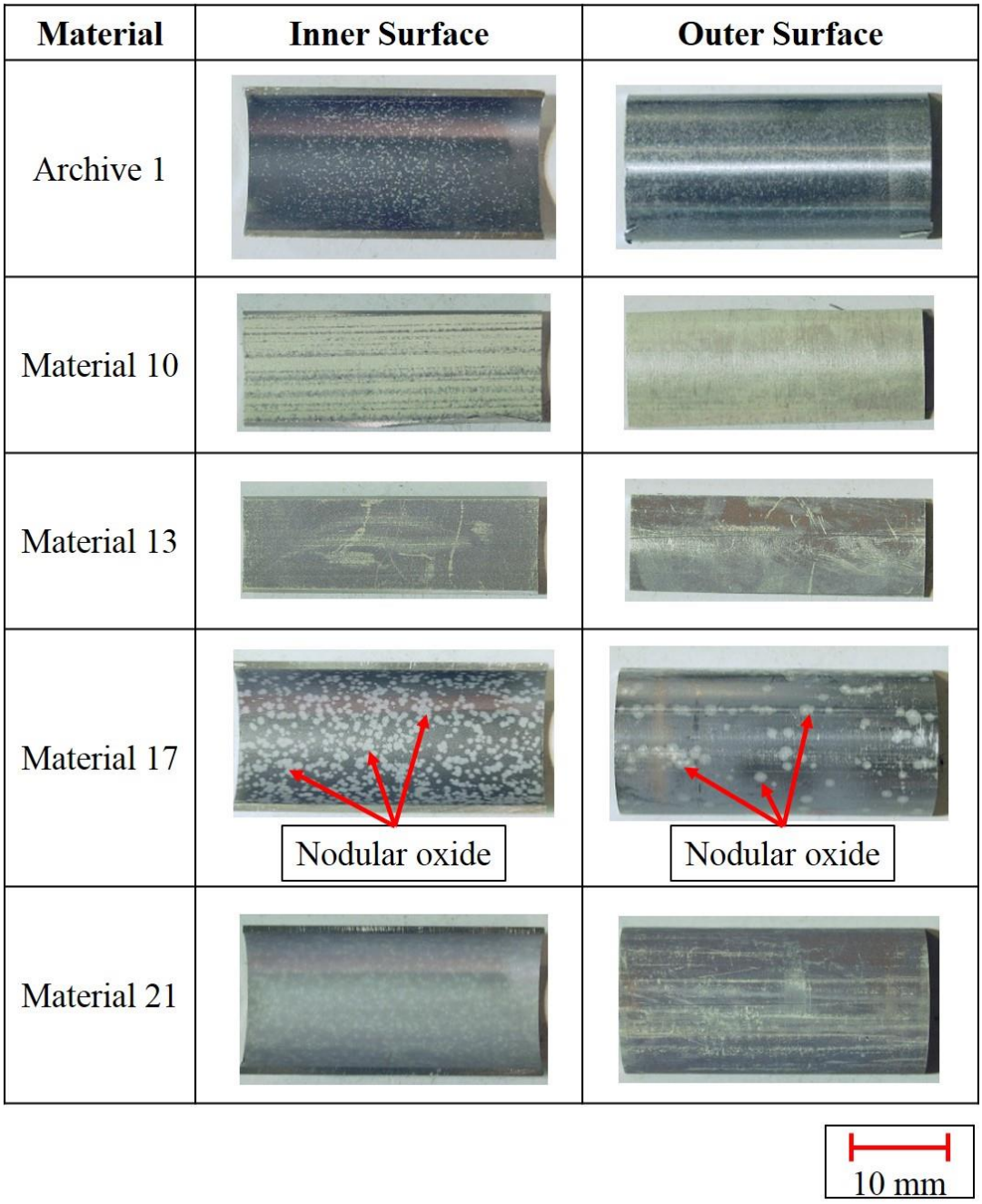

FIG. 2 Post irradiation pictures showing the appearance of irradiated, reactor-exposed, water rod samples. Nodules of oxide are present on the surface of Material 17, indicating the occurrence of nodular corrosion. Images courtesy of NFD.

SAMPLE PREPARATION

The samples for this study were shipped from GE-Hitachi's Vallecitos Hot Cell Facility to the LAMDA laboratory at Oak Ridge National Laboratory (ORNL), where they were prepared as cross-sectional samples in a manner similar to previous work and briefly reviewed here [11, 16-17].

Cross-sectional TEM samples were prepared from the bulk material containing both metal and oxide. Two-mm wide slices were cut from the bulk sample using a low-speed saw to yield one to two slices of each sample, depending on the availability of the material. These two slices were placed in a slotted molybdenum rod with a 2-mm diameter. This assembly was in-turn placed inside a ϕ3 mm brass tube. EPOTEK-353ND epoxy was used to hold this structure in place. The molybdenum rods and brass tubes were selected for use because the elements that comprise those components (molybdenum, copper, and zinc) do not have X-ray fluorescence lines that overlap with those of the elements of interest (zirconium, iron, chromium, and nickel). EPO-TEK 353ND epoxy was chosen based on known performance and reliability, as it has been used in previous experiments [15-16].

Once the epoxy set, slices approximately 500-μm thick were cut from the tubular structure. After being cut, the samples were polished using successively finer grit, starting at 600-grit (16-μm

particle size) and ending with 1-μm diamond solution. An example optical micrograph of a completed cross-sectional sample is shown in 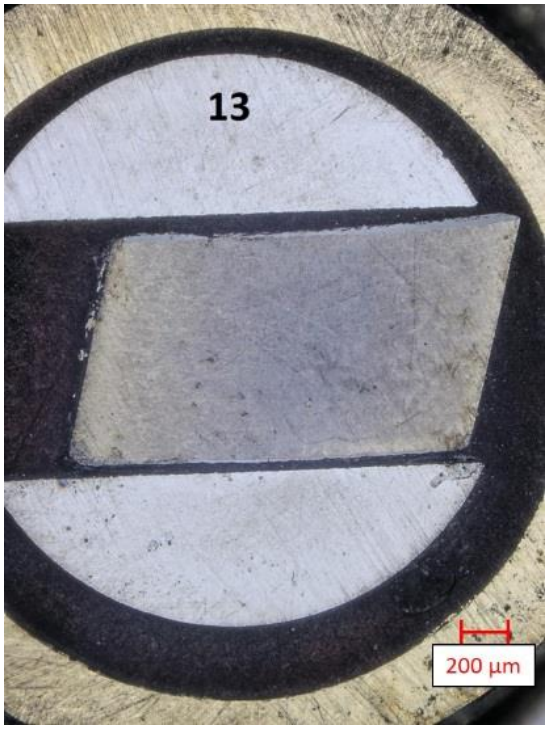

FIG. 3. Additionally, because samples were radioactive, they were encapsulated using 37-μm thick polyimide tubing for synchrotron radiation examinations.

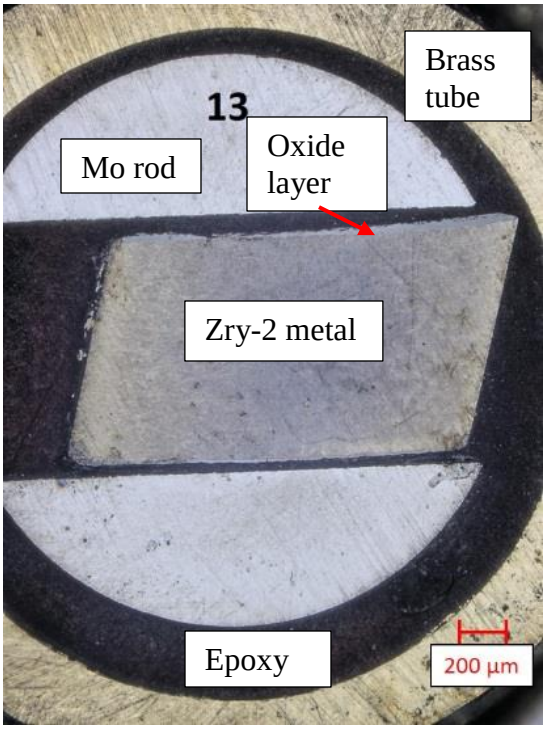

FIG. 3 Example cross-sectional sample prepared for microbeam synchrotron radiation examinations from irradiated water rod materials. Sample shown in figure was prepared from Material 13. Samples were prepared and imaged at the LAMDA lab at ORNL.

CHARACTERIZATION BY MICROBEAM XANES

X-ray absorption near-edge structure studies the absorption of X-rays in the sample within approximately 30 eV from the absorption edge [18-20]. When an atom absorbs a photon, the ejected photoelectron can scatter from the electrons of the neighboring atoms. When the photoelectron energy is low (i.e. X-ray energy just above the absorption edge), the photoelectron is more likely to scatter from the electrons of multiple atoms in the structure [19, 21]. After these scattering events, that photoelectron will be absorbed and the absorbing atom will emit a characteristic X-ray. Because the probability to re-absorb the photoelectron depends upon the availability of electronic states, the scattering events alter the intensity of the emitted characteristic

X-ray, which is measured in fluorescence XANES. As a result, the shape of a XANES spectrum gives information on the local structure of the element of interest including oxidation state, coordination geometry, and metal-ligand orbital hybridization [19-21].

Because the shape of a XANES spectrum depends on the local atomic structure and the oxidation state of the element of interest, one can expect a characteristic XANES spectrum for each element with a given electronic structure in a given phase. By characterizing and quantifying these differences, it is possible, in principle, to obtain the relative contributions of each phase present using well characterized standards. To that end, standards were acquired based on the phases expected in the samples. The standards used in this study for the iron and nickel edges are listed in **TABLE 3**. Powder standards were obtained from Sigma-Aldrich and Alfa Aesar. The $Zr(Fe,Cr)_2$ standard was obtained by arc melting the three elements together at the given stoichiometry. The spectra for nickel in Zircaloy-2 were obtained by performing XANES on unoxidized Zircaloy-2 channel material. The pure metal nickel and iron standards were obtained from the Hephaestus software, which is included in the Athena software package that was used for fitting [22]. These standards were modified for this data set by aligning edge positions to those of experimentally measured XANES spectra for fcc nickel and bcc iron powders; literature spectra and measured spectra were similar in shape and position, but literature standards were used due to their higher quality. The spectra for the experimental standards were later used in the oxidation state and linear combination fitting analyses.

TABLE 3 List of standards used for nickel and iron XANES examinations of Zircaloy-2.

Ni standards	Physical state	Origin
fcc nickel	Foil/powder	Hephaestus/Sigma-Aldrich
Nickel in Zry-2 metal	Bulk	Zircaloy-2 channel material
Nickel(II) oxide (NiO)	Powder	Sigma-Aldrich
Nickel(II,III) oxide ($Ni_{0.86}O$)	Powder	Alfa-Aesar
Nickel(III) oxide (Ni_2O_3)	Powder	Sigma-Aldrich
Nickel ferrite ($NiFe_2O_4$)	Powder	Sigma-Aldrich
Fe standards		
bcc iron	Foil/powder	Hephaestus /Sigma-Aldrich
Laves phase compound [$Zr(Fe,Cr)_2$]	Intermetallic compound	Arc-melted compound
Iron(II) oxide (FeO)	Powder	Sigma-Aldrich
Iron(II,III) oxide (Fe_3O_4)	Powder	Alfa-Aesar
Iron(III) oxide (Fe_2O_3)	Powder	Sigma-Aldrich
Nickel ferrite ($NiFe_2O_4$)	Powder	Sigma-Aldrich

SYNCHROTRON SETUP FOR MICROBEAM XANES

Microbeam XANES experiments were performed at the 2-ID-D beamline at the APS at Argonne National Laboratory. Using zone plate diffraction gratings, an X-ray beam size of 0.2 μm x 0.2 μm (FWHM) with a focal flux of 3×10^9 photons/second and an X-ray energy bandwidth (dE/E) of 0.01% is obtained. A schematic of the experimental setup is shown in **FIG. 4**. In this geometry, the microbeam was incident on the sample at 76° from the sample normal creating a footprint on the sample of 0.2 μm (normal to the oxide/metal interface) × 0.83 μm (parallel to oxide/metal interface). As a result of this geometry, the X-ray attenuation length into the sample was significantly reduced; using this geometry at 8.34 keV the attenuation length was 4.7 μm, whereas it would be 19.5 μm if the angle was 0° [23]. The sampling depth was considered to be three times this attenuation length, as this is the depth at which the X-ray intensity decreases by a factor of e^3 (approximately 95% attenuation). Because the beam footprint was an oval with a major axis diameter of 0.83 μm and a minor axis diameter of 0.2 μm, the volume sampled by the beam at a particular point was approximately 7.4 μm^3. If nickel-containing precipitates are assumed,

conservatively, to have a mean diameter of 200 nm and to be spherical, then the mean precipitate volume is approximately 4×10^{-3} μm^3, which is over three orders of magnitude smaller than the sampling volume. At the iron K-edge with 7.12 keV photons, the sampling volume is 4.8 μm^3, which is also three orders of magnitude larger than the precipitate volume. Because of this, the number of precipitates sampled by the beam was very large and it was not possible to distinguish between nickel and iron in solid-solution and in second-phase precipitates.

XANES signals were recorded in fluorescence, with a fluorescence detector placed near the sample normal. Each XANES scan probed the sample about the K-edge of the element of interest (8.34 keV for nickel and 7.12 keV for iron) with an energy window of ±40 eV and an energy step of 0.5 eV, which is sufficient to resolve peaked structures at these absorption edges [18]. Although the beam size changes as the energy is changed during a XANES scan, this change was approximately only 1-2%.

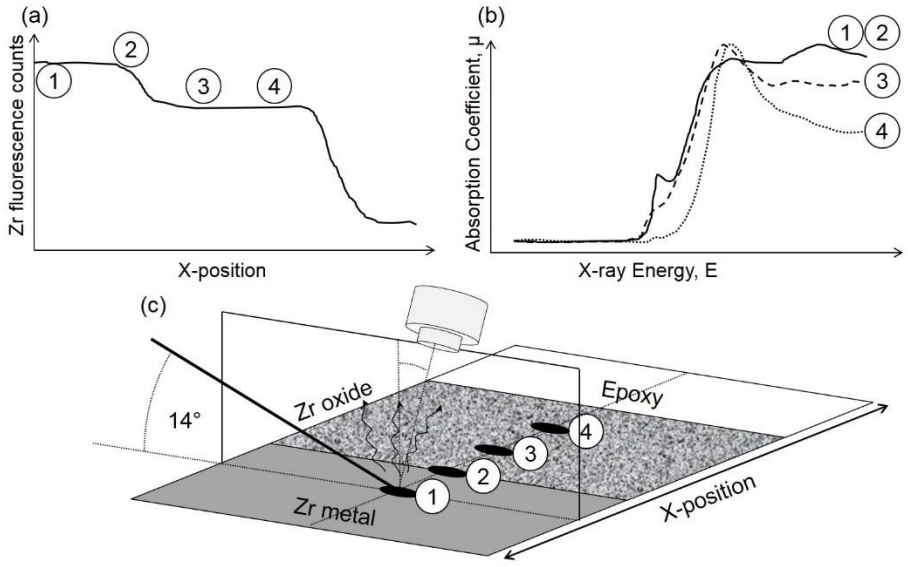

FIG. 4 Experimental setup for XANES experiments at the 2-ID-D beamline. As the scan moves from the metal into the oxide, (a) zirconium fluorescence and (b) XANES spectra are acquired. Numbered points in (a) and (b) are shown in (c).

For each sample, the location of the oxide layer was determined by performing a scan through the sample using zirconium L-edge fluorescence lines. As shown in **FIG. 4**, the plateau where zirconium fluorescence was the highest (1-2) was identified as the metal. The second plateau where zirconium fluorescence was slightly lower (3-4) was identified as the oxide layer. Similar fluorescence data for the other alloying elements were also collected. Once the oxide position had been determined, scans were set up to acquire XANES spectra at each point. Also at each point, zirconium fluorescence data was recorded to ensure that the sample remained properly aligned. Iron K-edge XANES spectra were acquired at 1.5 seconds/energy point over the 80 eV range with 0.5 eV step. Because of the low concentration of nickel in Zircaloy-2, data acquisition time was increased such that the number of counts in the XANES post edge region was at least 3,000. All data was normalized to the incident beam intensity. In the metallic region of the sample (1-2), nickel and iron XANES measured in this region remained unchanged, while in the oxide region of

the sample (3-4), XANES spectra began to change shape as nickel and iron began to transition from the metallic to the oxidized states.

ANALYSIS OF XANES SPECTRA

Once XANES data were acquired, they were imported into the Athena program for processing. The position of the absorption edge was calculated as the first position where the derivative of the fluorescence XANES absorption intensity with respect to energy was a maximum. **FIG. 5** plots XANES spectra and their respective derivatives for (a) fcc nickel and (b) nickel(II) oxide. Edge positions were calculated as 8332 eV and 8340 eV for fcc nickel and nickel(II) oxide, respectively.

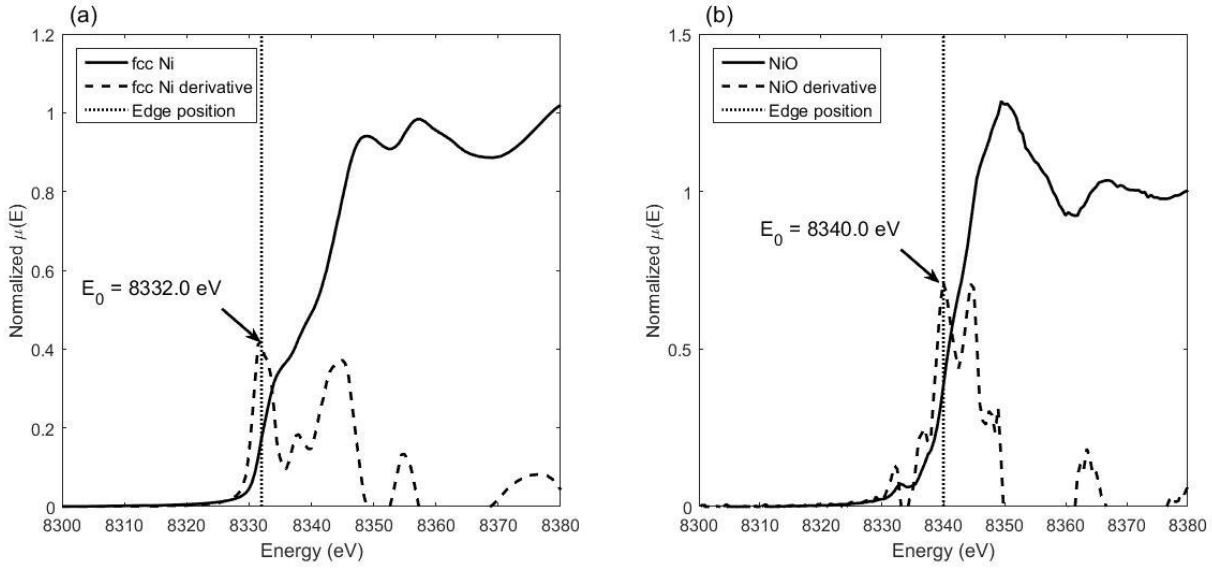

FIG. 5 Edge position of XANES spectra as defined by the first maximum of the first derivative (shown in dotted lines). (a) shows the XANES spectrum and derivative for fcc Ni and (b) shows the same for NiO.

After this step in the data analysis, a pre-edge function was fit to the region before the absorption edge (e.g. E < 8315 eV for nickel XANES) where absorption was minimal, while a post-edge function was fit to the region 15 eV past the edge position to the end of the acquired

spectrum. Once these fits were completed, the spectrum was flattened to remove differences in the post-edge region from the data; this is especially useful when performing linear combination fitting [22].

Linear combination fitting

Spectra from the examined samples were fit to linear combinations of the spectra obtained from XANES standards. Because the distinction between oxide phases and metallic phases was much more marked than among individual metallic and oxide phases (as illustrated in the following section) the sum of each type of standard (i.e. all oxide phases versus all metallic phases) was used as a measure of oxidation state at any given point. Thus, the fraction of metallic nickel or iron was used to characterize the oxidation state of the alloying elements as a function of distance from the oxide/metal interface.

Correlation of oxidation state with XANES edge position

Another analysis technique employed to examine the oxidation state of alloying elements was to relate XANES spectrum edge positions of the samples with those of the standard materials with known oxidation state, as described in other XANES examinations of transition metal oxides [24]. This was performed to estimate the actual oxidation state of alloying elements within the oxide layer. This analysis technique is considered complementary to the linear combination fitting, as XANES edge position is more sensitive to oxidation state than is the linear combination fitting.

Results

XANES SPECTRA

XANES spectra of the standard materials are shown in **FIG. 6**, where the normalized X-ray absorption coefficient is plotted as a function of energy for each standard material.

Typical nickel XANES spectra acquired in the different samples are shown in **FIG. 7** and typical iron XANES spectra are shown in **FIG. 8**.

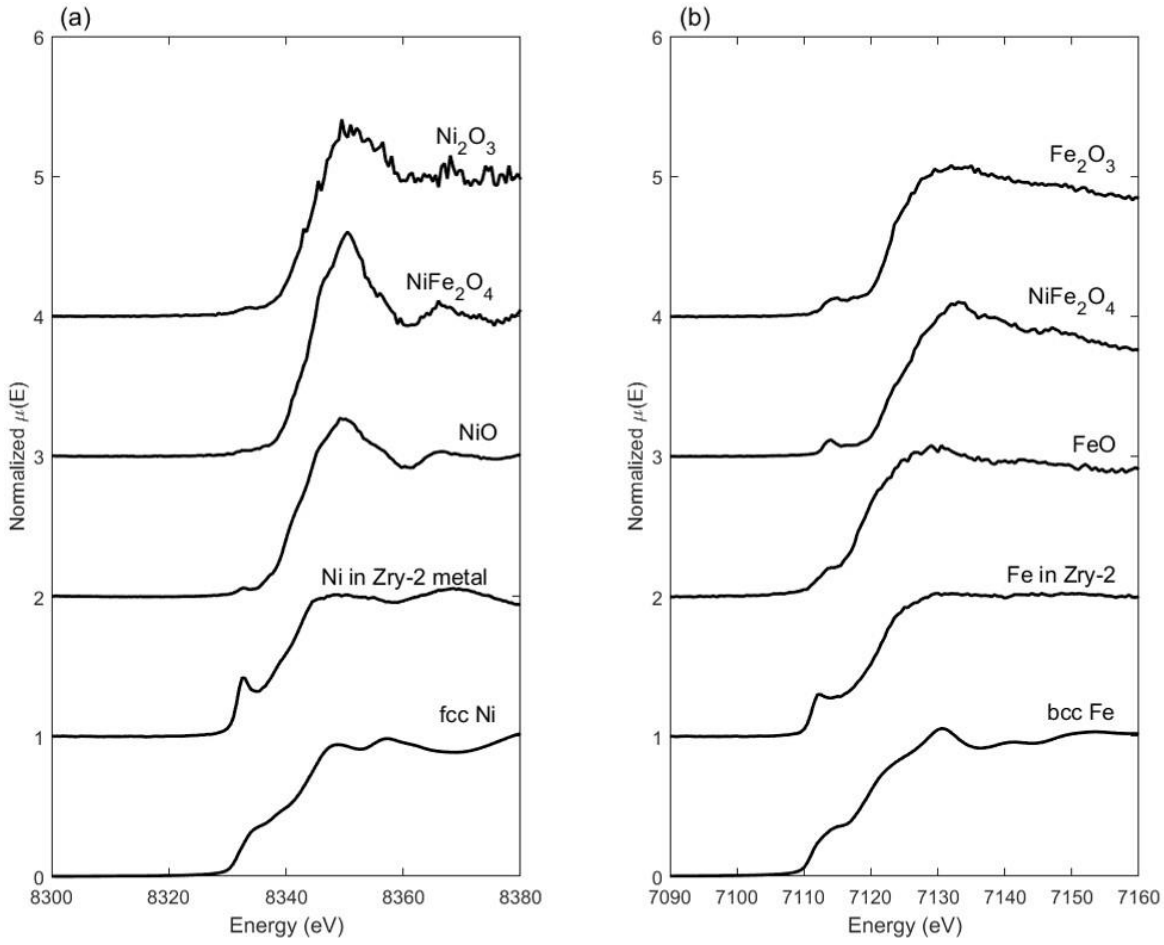

FIG. 6 XANES spectra of standard materials used for fitting the acquired spectra. (a) Nickel XANES standards. (b) Iron XANES standards.

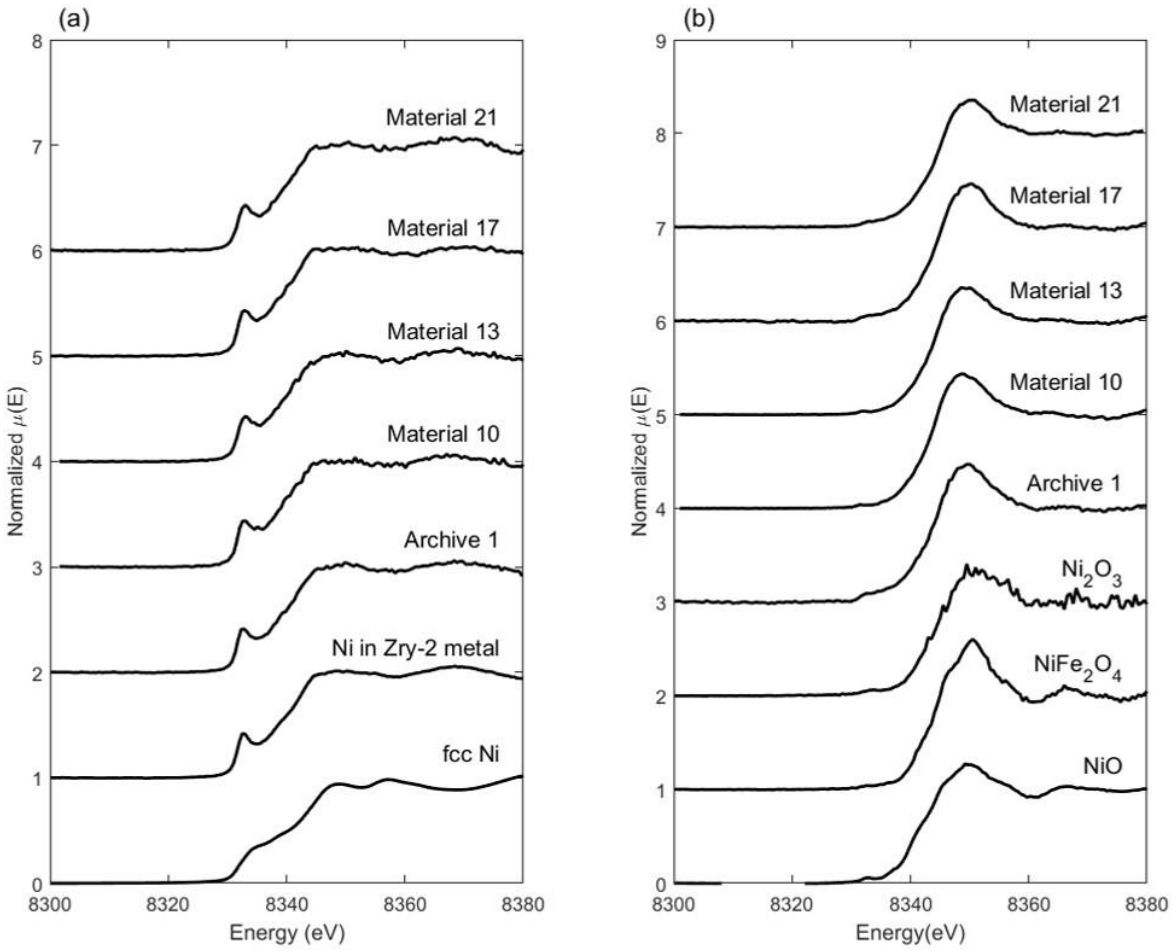

FIG. 7 Nickel XANES spectra acquired from standards and samples. (a) nickel XANES spectra from metallic standards and from the metal (far from the oxide/metal interface) of the analyzed samples. (b) nickel XANES spectra from oxide standards and from the bulk oxide (1 μm from the oxide/water interface) of the analyzed samples.

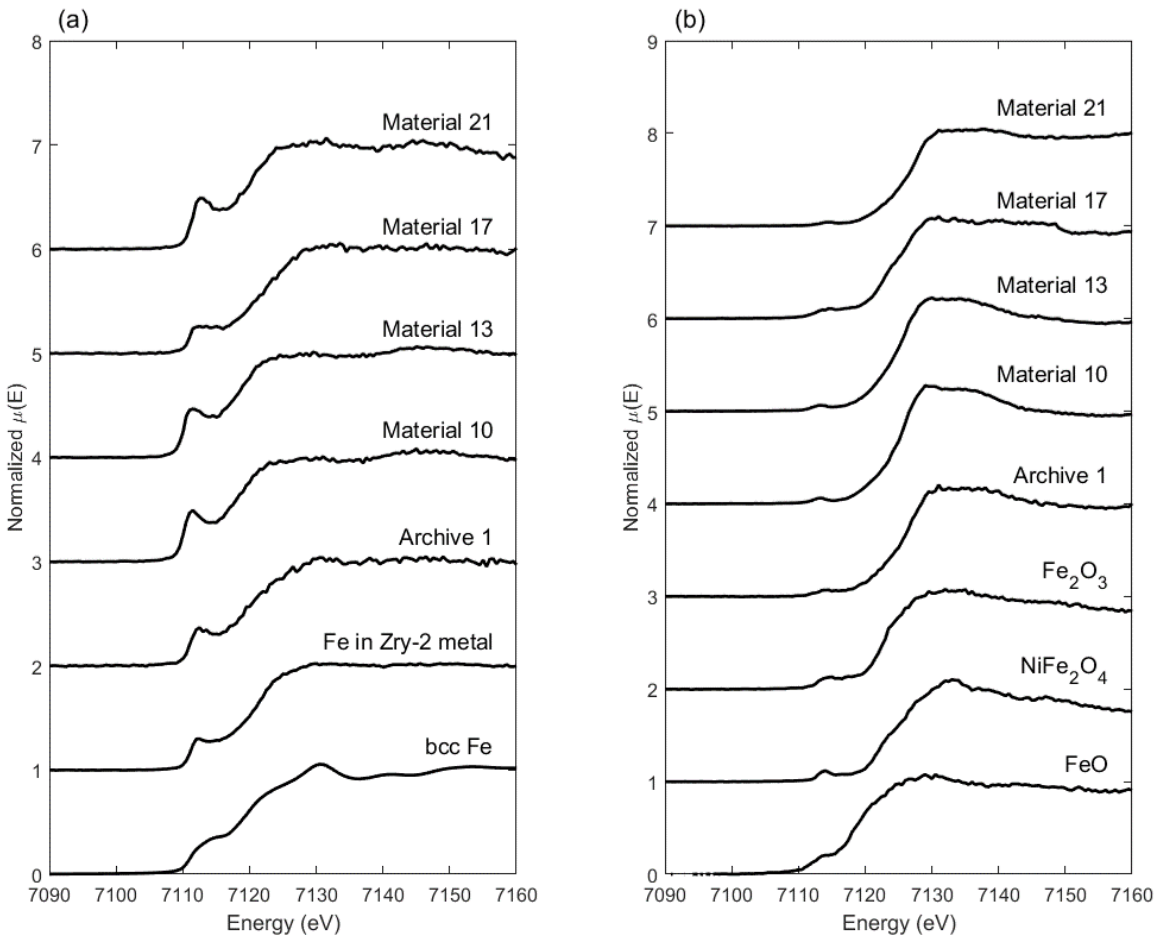

FIG. 8 Iron XANES spectra acquired from standards and samples. (a) iron XANES spectra from metallic standards and from the metal (far from the oxide/metal interface) of the analyzed samples. (b) iron XANES spectra from oxide standards and from the bulk oxide (1 μm from the oxide/water interface) of the analyzed samples.

FIG. 7 and **FIG. 8** plot normalized X-ray absorption coefficient as a function of energy for nickel and iron, respectively. **FIG. 7**(a) compares the fully metallic nickel XANES spectra of the samples with those of the metallic standards and **FIG. 7**(b) does the same for the fully oxidized XANES spectra and standards. The metallic spectra in **FIG. 7**(a) are quite similar and the same can be said of the oxide spectra in **FIG. 7**(b). **FIG. 8**(a) compares the fully metallic

iron XANES spectra of the samples with those of the metallic iron standards and **FIG. 8**(b) compares the fully oxidized XANES spectra and standards. As in **FIG. 7**, the metallic spectra in **FIG. 8**(a) are quite similar, as well as the oxide spectra in **FIG. 8**(b). Comparing the metallic and oxidized spectra of nickel and iron shows that spectra obtained in metallic Zircaloy-2 have a sharp feature at the metallic edge, located at 7112 eV for iron and 8333 eV for nickel, called a 'rising-edge feature' and a relatively flat post-edge at energies above 7130 for iron XANES and 8345 for nickel XANES. In contrast, oxidized spectra exhibit a low intensity 'pre-edge feature' at 7111.5 eV and 8332.5 eV for iron and nickel XANES, respectively, and a high intensity post-edge feature, often referred to as the 'white line', at 7130 eV and 8350 eV for iron and nickel XANES, respectively.

In order to better understand how XANES spectra changed shape and position as a function of oxide depth, the measured spectra at each spatial point in all samples was plotted, as shown in **FIG. 9** for nickel XANES and **FIG. 10** for iron XANES. These plots show the normalized X-ray absorption coefficient against X-ray energy and distance from the oxide/metal interface as determined by zirconium fluorescence and gives the evolution of the XANES spectra with oxide depth.

This type of analysis can be used to identify features that allow a qualitative evaluation of XANES measurements. For example, within a particular scan, it can be seen that in the metal the rising edge feature remains constant. As the scan moves into the oxide layer, the rising edge feature begins to decrease in intensity and reaches a constant, minimum value. At the same time, the post-edge intensity (white line) increases and then reaches an approximately constant maximum. These features have been shown previously to be good indicators of changes in oxidation state [12].

FIG. 9(a) shows the nickel XANES spectra for Archive 1 material. As one moves from the metal into the oxide layer, it is clear that the features described above associated with the metallic phase decrease, while those associated with the oxide phase grow. In particular, the rising-edge feature intensity, associated with metallic nickel, decreases, while the intensity of the large post-edge feature (white line), associated with oxidized nickel, increases. Not easily seen in this picture is the fact that the absorption edge position also moves to a higher energy level as the nickel is oxidized. This is, to first order, a Coulomb effect: higher oxidation states mean less charge on the atom, which results in less shielding of the nucleus. These changes in XANES features occur principally at the oxide/metal interface. However, it is noticeable in **FIG. 9** that the rising-edge feature characteristic of metallic nickel remains in the oxide layer for a considerable distance (several micrometers, at least) from the oxide/metal interface. This means that nickel does not oxidize immediately upon its incorporation in the oxide layer, with some metallic features remaining for approximately two μm. Note that Archive 1 and Material 17 oxide thicknesses were only 3.4 μm.

Nickel XANES spectra for Material 10 (**FIG. 9**(b)), and Material 17(**FIG. 9**(d)), show a similar permanence of metallic nickel spectrum characteristics that are clearly observed several micrometers into the oxide layer. In the thicker oxide layer of Material 10, nickel exhibits metallic character for up to five micrometers, while in Material 17, nickel exhibits metallic character for approximately three micrometers, which, in this case, is the whole oxide thickness. As nickel transitions from metallic to oxidized, the edge position of the XANES spectrum shifts to a higher energy.

XANES spectra for Material 13, shown in **FIG. 9**(c), and Material 21, shown in **FIG. 9**(e), also show metallic nickel at extended distances from the oxide/metal interface. In Material 13,

nickel shows metallic character for approximately fifteen micrometers (approximately half the oxide thickness), while in Material 21, nickel exhibits metallic character right up to the oxide/water interface. Thus, it is observed that, in the samples with higher hydrogen pick-up, nickel remained metallic further in the oxide layer as compared with those with lower HPUF.

FIG. 10(a) shows the iron XANES spectra for Archive 1. As for nickel XANES spectra, as one moves from the metal into the oxide layer, the metallic phase characteristics, particularly the rising-edge feature, decrease, while those of the oxide phase, such as the high post-edge intensity, grow. As before, the X-ray absorption edge shifts to higher energy as the iron oxidizes and this transition from metallic character to oxidized character occurs primarily near the oxide/metal interface. Iron also remains metallic for a distance into the oxide from the oxide/metal interface, typically on the order of about two micrometers in the thinner oxides of Archive 1 and Material 17, shown in **FIG. 10**(d), and on the order of five micrometers in thicker oxides of Materials 10, 13, and 21, shown in **FIG. 10**(b), **FIG. 10**(c), and **FIG. 10**(d), respectively. Thus, no significant difference in iron oxidation was observed when comparing between samples of low and high HPUF, and results are consistent with previous examinations of iron in Zircaloy-4 corroded in steam [12].

It should be noted that, for thinner oxides, points were evenly spaced using a step of at least 0.25 μm. The thick oxide layers were probed using a 1.0-μm step and a finer (0.25 μm step) mesh in the region near the oxide/metal interface.

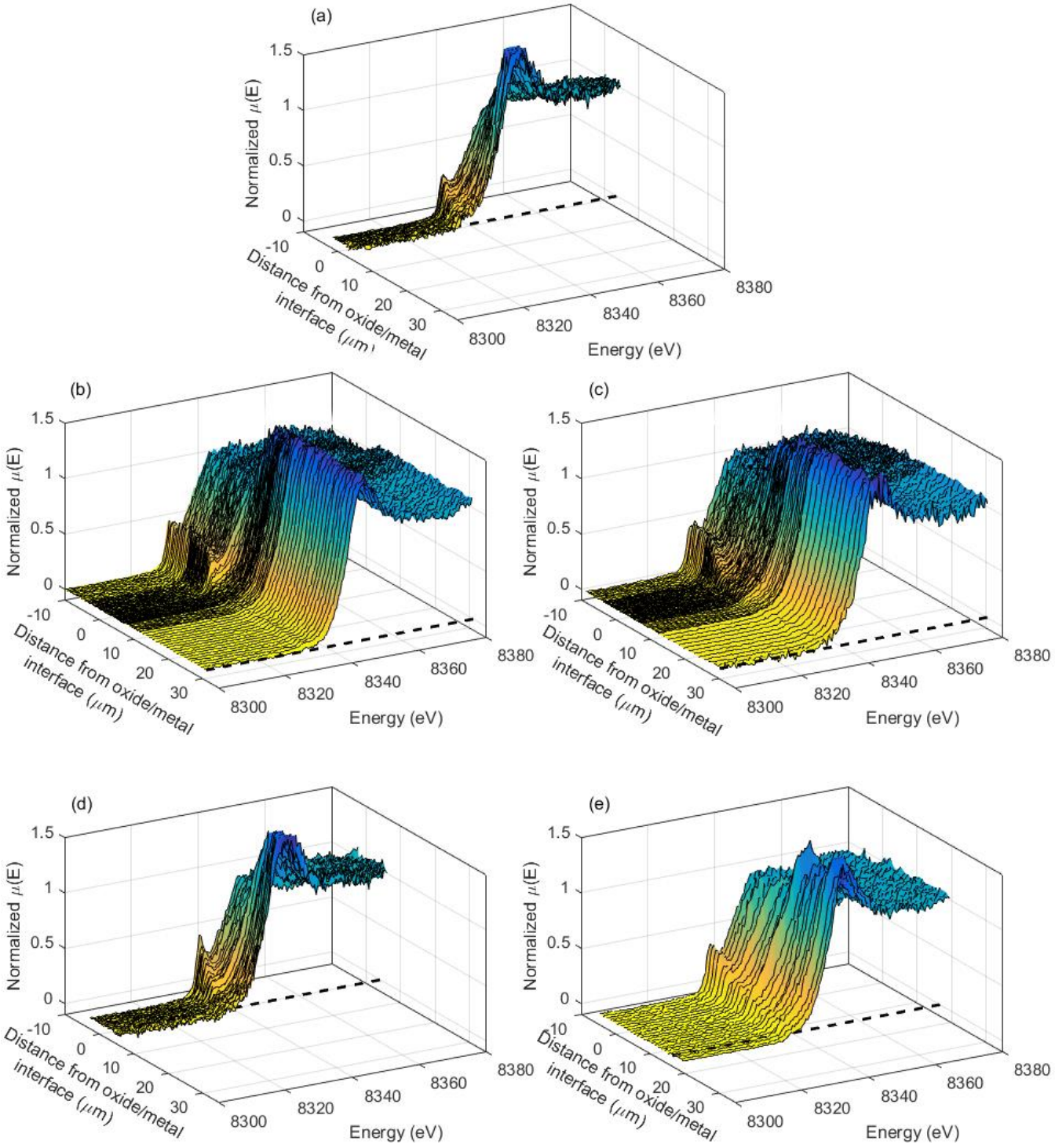

FIG. 9 Plots of Ni XANES spectra as a function of distance from the oxide/metal interface. (a) Results for Archive 1. (b) Results for Material 10. (c) Results for Material 13. (d). Results for Material 17. (e) Results for Material 21. Results are all plotted to reflect the same length scale. The dotted line shows the location of the oxide/water interface for each sample.

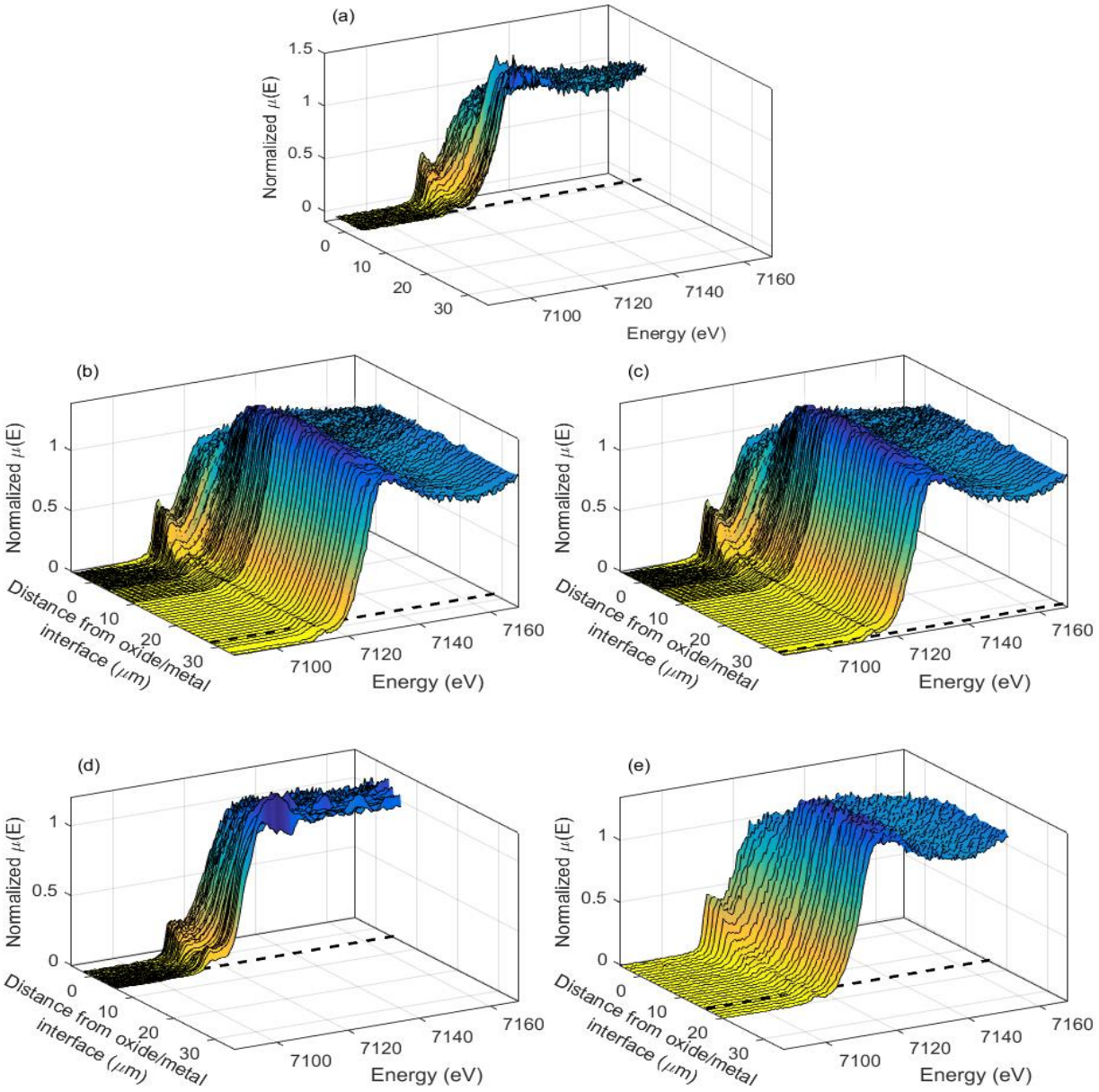

FIG. 10 Plots of Fe XANES spectra as a function of distance from the oxide/metal interface. (a) Results for Archive 1. (b) Results for Material 10. (c) Results for Material 13. (d). Results for Material 17. (e) Results for Material 21. Results are all plotted to reflect the same length scale. The dotted line shows the location of the oxide/water interface for each sample.

LINEAR COMBINATION FITTING

A linear combination of the standard spectra was fit to the XANES spectra measured at a particular point in a sample. This was done for both nickel and iron XANES examinations of all samples using the standards detailed in **TABLE 3**. Example fits of nickel XANES spectra acquired from Material 10 are shown in **FIG. 11**. For each of these plots, the circles correspond to the acquired spectra and the solid lines correspond to the linear combination fitting. The dashed curves correspond to the sum of metallic standards and the dotted curves correspond to the sum of oxidized standards. Each fit has an associated R-factor and fits. The fits all have R-factors < 0.01. The spectrum in **FIG. 11**(a) was acquired in the metal far from the oxide metal interface and it is clear that the fitting can be very well accomplished using only metallic standards. This is not the case for the spectrum in **FIG. 11**(b), acquired in the oxide, not far from the oxide/metal interface, which can only be fitted with a combination of oxide and metal standards, as shown. Finally, the spectrum in **FIG. 11**(c) was acquired far from the oxide metal interface into the oxide and can be fit using only oxide standards.

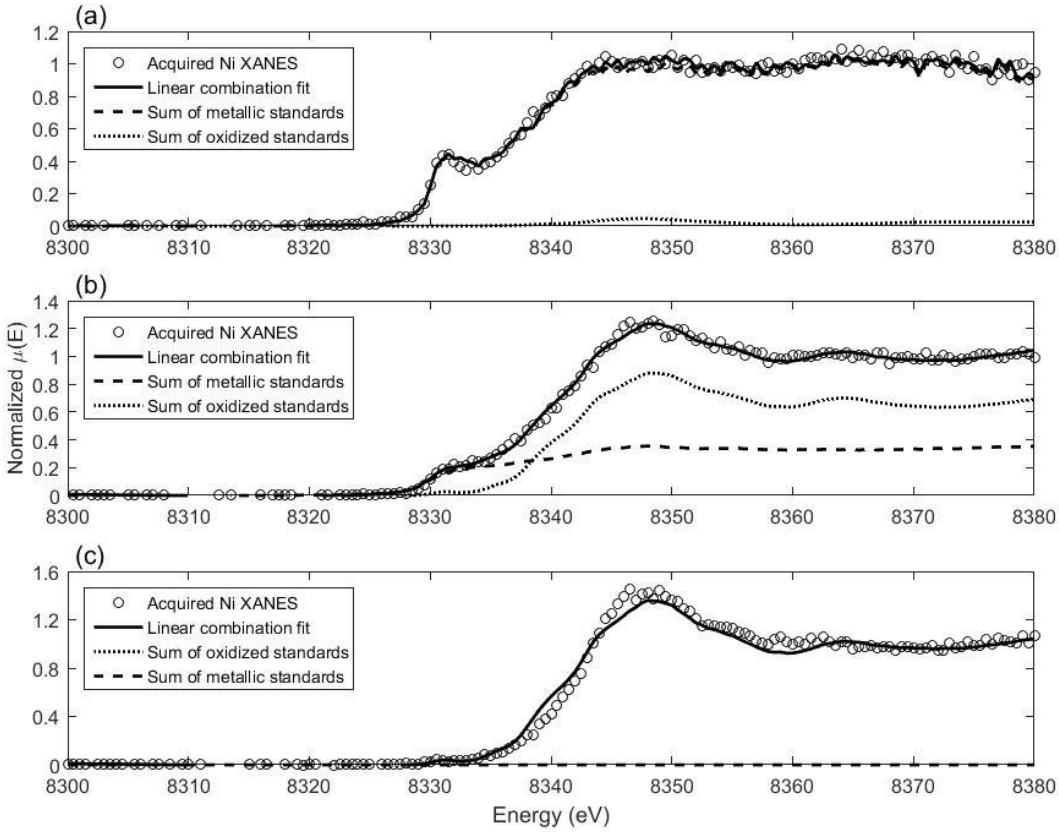

FIG. 11 Nickel XANES linear combination fitting results for various points in Material 10. (a) Fitting results 10.2 μm from the oxide/metal interface in the metal. (b) Fitting results 2.8 μm from the oxide/metal interface in the oxide layer. (c) Fitting results 19.8 μm from the oxide/metal interface in the oxide layer.

The fraction of metallic nickel at different locations in the oxide layer calculated from the sums of all oxide and metal phases is shown in **FIG. 12** and **FIG. 13**. The metallic nickel fraction is presented in **FIG. 12**(a) for each of the five samples examined. The oxide thicknesses are also indicated in each case. **FIG. 12**(b) shows the same data expanded near the oxide/metal interface.

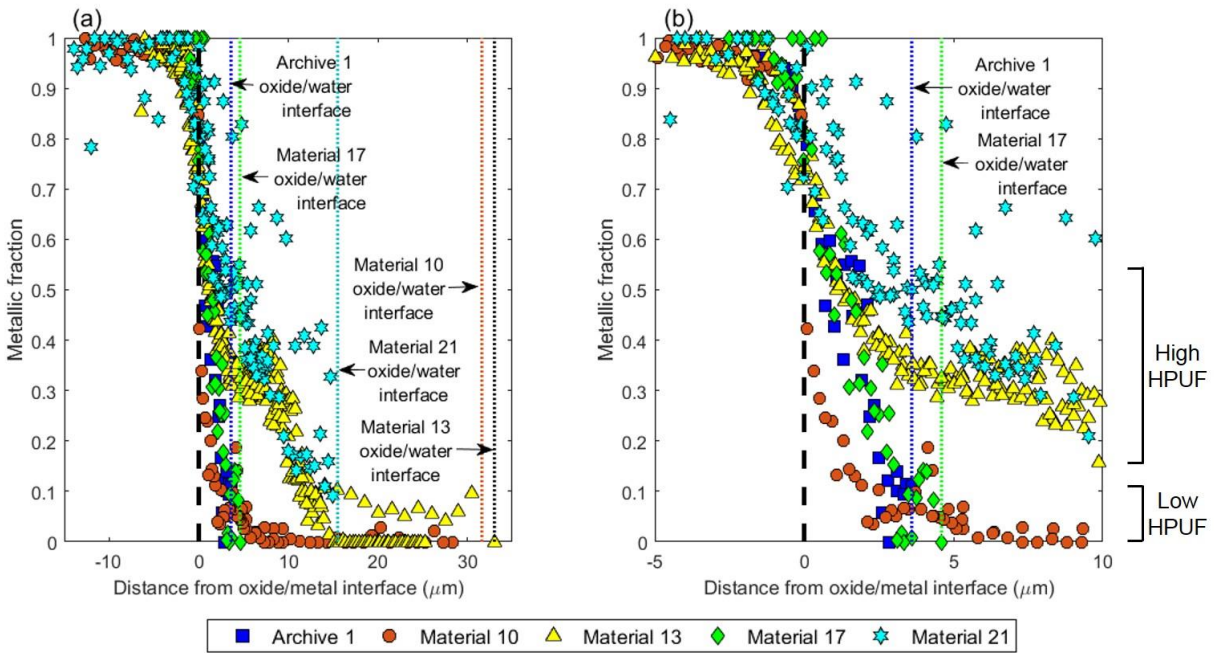

FIG. 12 Plot of metallic Ni weight fraction as a function of distance from the oxide/metal interface for each of the examined samples. (a). Shows the linear combination fitting results over the whole oxide thickness range, while (b) focuses on 15 µm around the interface.

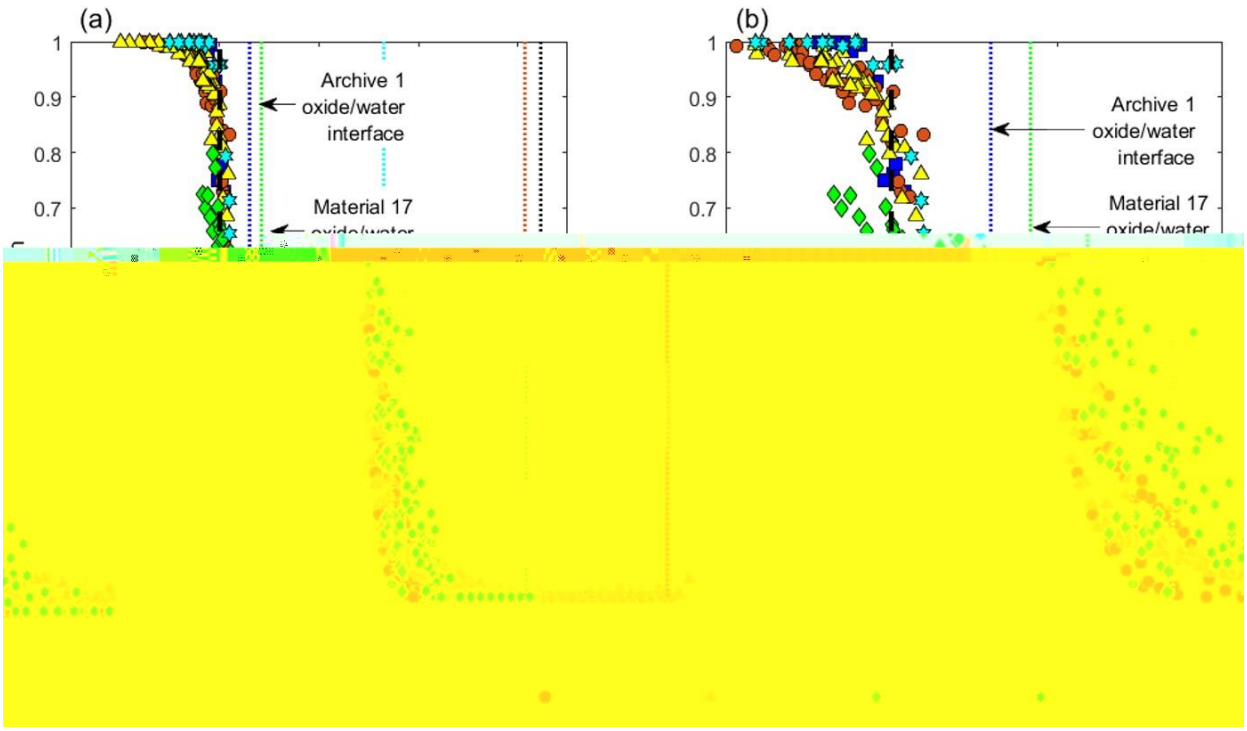

FIG. 13 Plot of metallic Fe weight fraction as a function of distance from the oxide/metal interface for each of the examined samples. (a) shows the linear combination fitting results over the whole oxide thickness range, while (b) is an expanded view of the 15 μm near the oxide/metal interface.

The plots in **FIG. 12** indicate that in all samples studied nickel exhibited delayed oxidation relative to the host zirconium and remains metallic into the oxide layer. The percent metallic nickel is much higher in the oxide layers associated with high HPUF (Materials 13 and 21) than in those associated with low HPUF (Archive 1 and Materials 10 and 17). This suggests that the presence of metallic nickel is important to increased HPUF. It is also apparent that, in Archive 1, Material 17, and Material 10, nickel became fully oxidized in under ten micrometers from the oxide/metal interface, while in Materials 13 and 21 (high HPUF), nickel remained partially metallic for a significant portion of the oxide thickness. In Material 13, nickel remained greater than 10% metallic for approximately fifteen micrometers away from the oxide/metal interface, while in

Material 21, nickel only fully oxidized near the oxide/water interface. These fitting results were consistent with the evolution of the XANES spectra that was shown in **FIG. 9**.

FIG. 13 plots the same data, but for the iron metallic fractions over the same set of samples. As in **FIG. 12**, **FIG. 13**(a) shows the data over the full range of oxide thickness and **FIG. 13**(b) shows the same data over a region closer to the oxide/metal interface. **FIG. 13** shows that the oxidation of iron is delayed relative to that of zirconium, but earlier than that of nickel in each case. The remarkable observation is that iron shows no consistent difference in oxidation state between samples with high and low HPUF. In Archive 1, iron fully oxidized within two micrometers from the interface and in Materials 10 and 21, iron fully oxidized within five micrometers. In Material 13, iron reached full oxidation by ten micrometers from the interface. From these results, it was clear that (i) nickel remained metallic longer than iron did and (ii) longer in materials with high HPUF, while iron oxidation behavior between samples with high and low HPUF was relatively similar. Some metallic iron was observed near the oxide/water interface in Material 17 data and was assumed to be due to the presence of iron from CRUD, which was mischaracterized as metallic iron. This was because CRUD typically has a high concentration of iron, causing large detector dead times and misshapen XANES spectra due to self-absorption [25]. A similar, though smaller, variation in nickel signal of Material 17 was also seen.

OXIDATION STATE ANALYSIS

The edge position as determined from the inflection point of the XANES spectrum is not used extensively in the linear combination fitting process, but can be a more sensitive gauge of the oxidation state, since analysis of oxidation state from XANES edge position is independent of linear combination fitting. As described earlier, this analysis was performed by correlating the oxidation state of a standard with its XANES spectrum edge position. In this analysis taking the

edge of a particular spectrum as the maximum of the first derivative of the XANES spectrum, the edge energy was determined for each location in each sample. A table of standards, their oxidation state, and their XANES edge positions are shown in **TABLE 4**. Plots of oxidation state as a function of XANES edge position and best fit lines for these plots are given in **FIG. 14**. The calibration curve for nickel standards is shown in **FIG. 14**(a) and for iron standards in **FIG. 14**(b).

TABLE 4 List of XANES standards used for the calibration curve, their oxidation states, and their XANES edge positions with respective 95% confidence intervals (CI).

Nickel standards			Iron standards		
Standard	**Oxidation state**	**Edge position (eV) ± 95% CI**	**Standard**	**Oxidation state**	**Edge position (eV) ± 95% CI**
fcc nickel	0+	8331.9 ± 0.3	bcc iron	0+	7110.8 ± 1.0
Nickel in Zry-2 metal	0+	8331.0 ± 0.5	Laves phase $Zr(Fe,Cr)_2$	0+	7111.0 ± 0.2
Nickel(II) oxide (NiO)	2+	8340.0 ± 0.4	Iron (II) oxide (FeO)	2+	7117.9 ± 0.8
Nickel (II,III) oxide ($Ni_{0.86}O$)	2.32+	8344.1 ± 0.2	Iron(III) oxide (Fe_2O_3)	3+	7122.8 ± 0.9

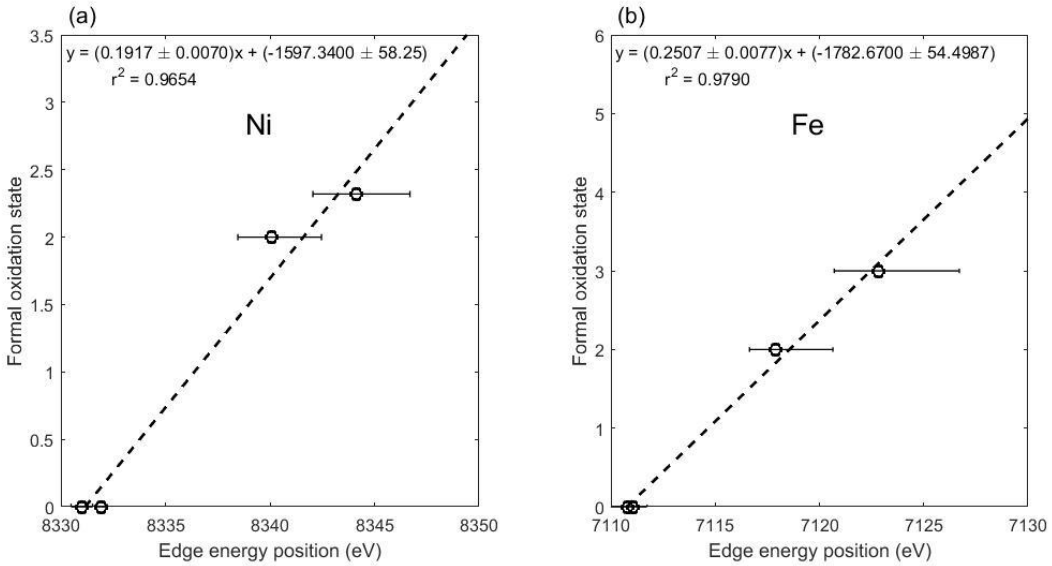

FIG. 14 Relation between oxidation state of standard materials to their XANES edge position. Standards used are the ones listed in **TABLE 4**. (a) shows this this relation for nickel standards and (b) shows the relation for iron standards. Error bars are 95% confidence limits of edge energy position.

XANES edge positions in each of the XANES spectra at each point in each examined sample were calculated. The results of this analysis are shown in **FIG. 15**.

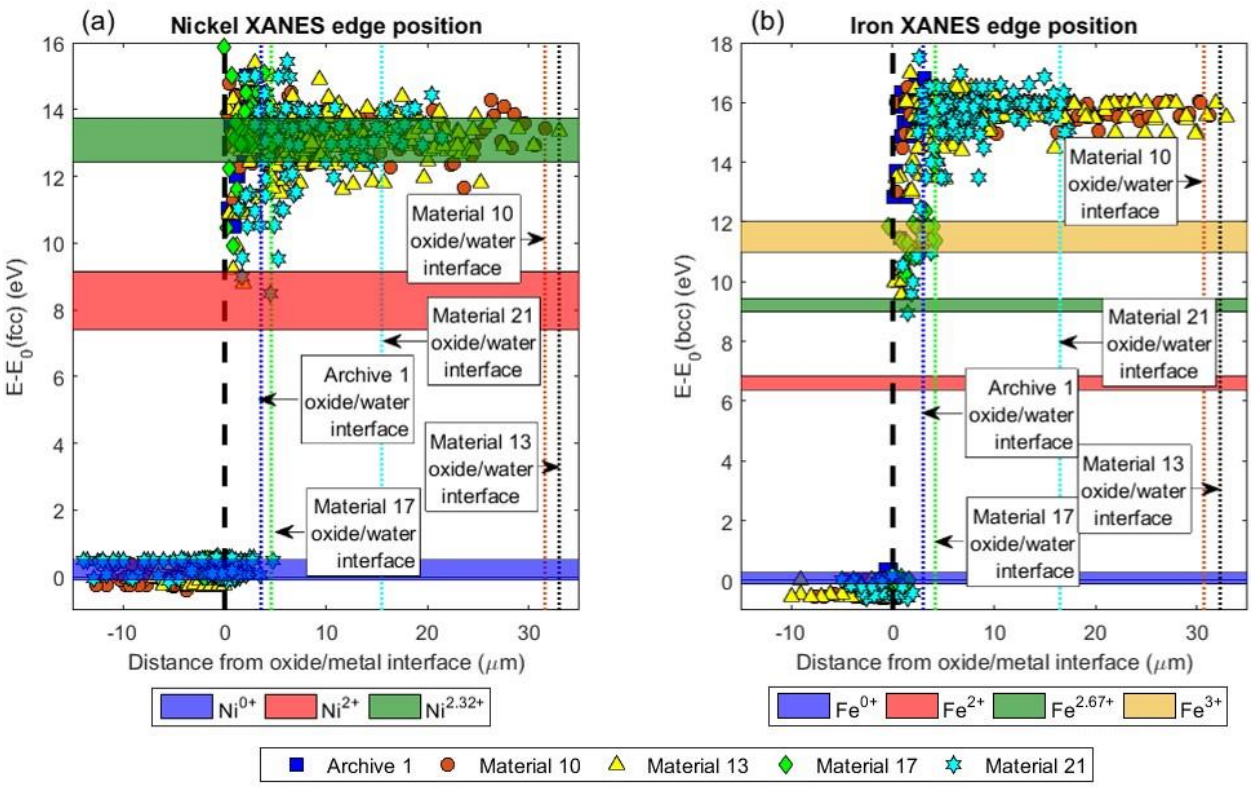

FIG. 15 XANES edge energies of (a) nickel and (b) iron as measured using the maximum of spectrum derivative. Boxed regions show edge position ± 95% confidence intervals for standard materials.

FIG. 15(a) plots nickel XANES edge position as a function of distance from the oxide/metal interface. It is seen that, in all samples, nickel oxidizes to an oxidation state near 2+ (shown in the red band) around the oxide/metal interface, then, further into the oxide layer, to approximately 2.3+, which corresponds to a mixture of 70% NiO and 30% Ni_2O_3.

FIG. 15(b) plots iron XANES edge energy as a function of oxide depth. Iron appears to oxidize to approximately the 3+ state (shown as the green band) near the oxide/metal interface, then oxidize to a higher oxidation state, possibly 4+, further away. The only sample that this was not the case for was Material 17, in which iron remained in the 3+ state throughout the thin oxide layer.

Discussion

The above results show a link between the oxidation behavior of nickel once incorporated into the oxide layer and accelerated hydrogen pick-up at high burn-up.

RELATIONSHIP BETWEEN DELAYED OXIDATION OF ALLOYING ELEMENTS AND HYDROGEN PICK-UP

Both nickel and iron exhibit delayed oxidation relative to the base zirconium. The delayed oxidation of iron is in agreement with previous examinations of Zircaloy-4 oxide layers using both electron microscopy and XANES [11-12, 26-29]. Based on the work by Pêcheur, et al., it is believed that there are different domains of stability for zirconium, iron, and chromium in the metallic state in the dense oxide layer. Thus, when precipitates are initially incorporated into the oxide layer, they remain metallic, as they are more thermodynamically noble than the base zirconium metal [14]. As the oxide grows inward, the partial pressure of oxygen experienced by the metallic precipitate begins to increase, causing the oxidation of (in order) zirconium, chromium, and iron [26]. Extending this argument to include nickel indicates that nickel will remain metallic longer than the other alloying elements, as it is known to be more thermodynamically immune to corrosion in water than the other elements in zirconium-based alloys [30]. This is consistent with observations in this experiment, which showed that nickel did, in fact, remain metallic longer than did iron, as shown by a comparison of **FIG. 12** and **FIG. 13**. It should be noted that, since these measurements were performed in 500-µm-thick samples, it was not possible to distinguish the contributions of nickel and iron in solid-solution from that of nickel and iron in precipitates [11].

Comparing the results of iron oxidation behavior in this study to the results of previous examinations of iron in autoclave-corroded Zircaloy-4 shows that iron in BWR-corroded Zircaloy-2 remains metallic for up to 5 μm past the oxide/metal interface into the oxide layer, while iron in autoclave-corroded Zircaloy-4 remains metallic up to approximately 1.5 μm in 360 °C water, and five to six micrometerss in 400 °C steam [11-12]. Ensor et al. hypothesized that iron remained metallic longer in steam-corroded samples than in water-corroded samples because, for a given oxide thickness, the faster corrosion kinetics at higher temperatures allow less time for iron to oxidize [12]. For the samples examined in this study, no clear effect of iron oxidation on hydrogen pick-up is discernable.

A consistent difference is seen in the oxidation behavior of nickel between low- and high-HPUF materials. A comparison of metallic nickel fraction in Materials 10 (low HPUF) and 13 (high HPUF) shows that nickel remains metallic longer in Material 13 than in Material 10. Although in Material 10 nickel begins to oxidize later than iron, both elements become fully oxidized at approximately the same point, which is 5 μm from the oxide/metal interface in the oxide layer. In Material 13, both nickel and iron begin to oxidize at approximately the same point, which corresponds to the oxide/metal interface. However, while iron behaves in a similar manner as in Material 10, nickel remains partially metallic for more than 10 μm past the oxide/metal interface into the oxide layer.

A comparison between Materials 17 (low HPUF) and 21 (high HPUF) yields a parallel to the previous comparison. In Material 17, the oxidation behaviors of iron and nickel are similar, as they are in Material 10. In Material 21, iron and nickel begins to oxidize at the same point, close to the oxide/metal interface. However, while iron reaches approximately complete oxidation at approximately 5 μm from the oxide/metal interface, nickel remains partially metallic for more than

10 μm past the interface. From these results, it is clear that nickel remains metallic in the high HPUF samples for a thickness larger than protective oxide layer, which is typically between two to three micrometerss in Zircaloy-2 corroded in a steam environment [8]. Thus, metallic nickel would be present in the porous oxide layer, allowing the corrosion medium access to the metallic nickel. Because of this, it is hypothesized that metallic nickel acts as a catalyst for surface reactions that result in hydrogen ingress from the coolant to the protective oxide layer. However, the mechanism by which nickel remains metallic to such distances in the oxide layers of high HPUF samples is not fully understood.

Examination of results from Archive 1 shows that nickel becomes fully oxidized approximately 2.5 – 3 μm from the oxide/metal interface, while iron becomes fully oxidized within 2 μm of the interface. This analysis suggests that delayed oxidation of nickel in the zirconium oxide layer plays a role in accelerated hydrogen pick-up of Zircaloy-2 at high burn-up. In particular, samples with significantly delayed oxidation of nickel exhibit high hydrogen pick-up.

The observations shown here raise the question of how nickel affects hydrogen pick-up in zirconium alloys. The possibility of metallic nickel enhancing hydrogen transport in the oxide layer has been raised by some researchers, as the presence of a metallic nickel "short-circuit" could allow easier hydrogen ingress [7]. However, such a short-circuit path would also lead to easier electron transport from the metal out of the oxide layer, which would cause hydrogen evolution at the oxide/water interface, thus reducing hydrogen pick-up [15, 31-32]. One possibility is that the presence of metallic nickel in the outer portion of the protective oxide layer and at the pore surfaces of the non-protective oxide could enhance hydrogen ingress into the oxide, thus acting as a catalyst for the surface reaction. This could be consistent with higher hydrogen pick-up in samples where metallic nickel is present in larger quantities at larger distances in the oxide layer.

CHEMICAL STATE OF ALLOYING ELEMENTS UPON INCORPORATION INTO OXIDE LAYER

Because previous investigations of SPP corrosion behavior in Zircaloy-4 saw evidence for the presence of bcc iron [26], nickel and iron XANES spectra were fit to include fcc nickel and bcc iron as standards. The case of fcc nickel is shown in **FIG. 11**(b). This suggests the presence of a phase akin to fcc nickel, as well as bcc iron in the samples. In fitting the XANES spectra in the oxide, it is often found that the inclusion of fcc nickel and/or bcc iron as standards is essential to achieving a good fit. Fitting weights for these standards are especially high near the region where nickel and iron transitioned from the metallic to the oxidized state. In the metal, although bcc iron and fcc nickel standards can be included with small fitting weight fractions in the fit, they are not necessary. In analyzing the fluorescence spectra acquired above the nickel K-edge from scans of the oxide layer, it was noticeable that iron peaks were normally found near both chromium and nickel peaks, suggesting the presence of precipitates in those locations. An increase in nickel fluorescence countrate was also correlated with the presence of 'fcc' nickel, in qualitative agreement with the determination of bcc iron in ZrCrFe precipitates in the oxide layer [26], though it was not possible to make a definitive assignment of fcc nickel to the presence of precipitates.

From the results of the oxidation state analysis of nickel, it appears that nickel oxidizes to approximately the 2.3+ state, corresponding to a mixture of 70% NiO and 30% Ni_2O_3. The correlation between oxidation state and edge position for iron shows that, in Archive 1 and Materials 10, 13, and 21, the oxidation state is approximately 3+ near the oxide/metal interface and a higher state further into the oxide layer. This suggests that iron initially corrodes to Fe_2O_3 in the oxide layer and then forms a mixture of phases, such as Fe_2O_3 and FeO_2.

Previous work predicted that, in oxidizing conditions in the zirconium oxide layer, the stable oxidation states for nickel and iron were both 3+ [34]. However, FeO_2 has been observed in studies of the oxidation of iron metal in an oxygen doped argon matrix under UV irradiation, and other, similar oxides, such as Fe_2O_4, Fe_2O_5, and Fe_2O_6, have been reported to form during interaction between laser-ablated iron and oxygen, thus showing that iron is capable of oxidizing up to the 6+ state, albeit under extreme conditions [35-36].

Conclusion

A focused set of neutron-irradiated Ziraloy-2 water rod samples was examined to highlight the differences that lead to accelerated hydrogen pick-up at high burn-up. Measurements of nickel and iron oxidation state as spatially resolved within the oxide depth were conducted using microbeam synchrotron radiation XANES for each of these samples. Measured XANES spectra were compared with spectra of standard materials to obtain information on the oxidation behavior of iron and nickel once incorporated into the oxide layer. The main conclusions are:

1. Zirconium, iron, and nickel oxidized in this order, consistent with Pourbaix diagrams of the three elements, in which nickel is ranked as the most thermodynamically noble of the three elements and zirconium is the least noble.
2. In samples with low HPUF, nickel began to oxidize later than did iron, but both reached approximately full oxidation near the same position. In contrast, in the samples with high HPUF, nickel and iron both began to oxidize at the same point. Iron oxidized in a similar fashion in both low and high HPUF materials, while nickel remained partially metallic for significant portions of the oxide thickness in high HPUF materials. This suggests that the

presence of metallic nickel in the non-protective oxide layer could be a reason for higher hydrogen pick-up in these alloys.

3. The oxidation state of nickel in the oxide layers was determined to be approximately 2+ near the oxide/metal interface and approximately 2.3+ further into the oxide layer, suggesting a mixture of 70% NiO and 30% Ni_2O_3. In contrast, iron initially oxidized to 3+, increasing later in the oxide layer. Linear combination fitting results fcc nickel and bcc iron in the oxide near the region where nickel and iron oxidize.

ACKNOWLEDGEMENTS

This research was performed under the auspices of the EPRI-led Nuclear Fuel Industry Research (NFIR) Program. The authors acknowledge the technical input from NFIR members and thank them for permission to publish the results. The authors acknowledge the resources provided by 2-ID beamline staff and APS safety officers, especially W. VanWingeren, for accommodations to examine radioactive samples at the 2-ID-D beamline. The authors thank the staff at Vallecitos Nuclear Center for shipping radioactive samples to ORNL for preparation, and acknowledge the resources provided by staff at the LAMDA laboratory at ORNL, including J. Busby and I. Dunbar for help in preparing samples and shipping them to APS. The authors thank A. Couet, K. Sakamoto, G. Kuri, N. Ramasubramanian, F. Garzarolli, M. Newville, and B. Ravel for helpful discussions. Finally, the authors thank B. Ensor, E. Lacroix, and E. Alat for their assistance in performing experiments at the APS. This research used resources of the Advanced Photon Source, a U.S. Department of Energy (DOE) Office of Science User Facility operated for the DOE Office of Science by Argonne National Laboratory under Contract No. DE-AC02-06CH11357.

REFERENCES

[1] Lustman, B. "Zirconium Technology - Twenty Years of Evolution," *ASTM Special Technical Publication,* ASTM STP 681, 1979, pp. 5-18.

[2] Kass, S. "Development of Zircaloys," *Corrosion of Zirconium Alloys, ASTM STP 3687,* ASTM International, Philadelphia, PA, 1964, pp. 3-27.

[3] Yeniscavich, W.; Wolfe, R. A.; Lieberman, R. M. "Hydrogen Absorption by Nickel Enriched Zircaloy-2," *Journal of Nuclear Materials,* 1, 3, 1959, pp. 271-280, doi: 10.1016/0022-3115(59)90023-6.

[4] Harada, M.; Kimpara, M.; Abe, K. "Effect of alloying elements on uniform corrosion resistance of zirconium-based alloys in 360 °C water and 400 °C steam," *9th International Symposium on Zirconium in the Nuclear Industry,, ASTM STP 1132,* ASTM International, West Conshohocken, PA, 1991, pp. 368-390.

[5] Broy, Y.; Garzarolli, F.; Seibold, A.; Swam, L. F. V. "Influence of Transition Elements Fe, Cr, and V on Long-Time Corrosion in PWRs," *12th International Symposium on Zirconium in the Nuclear Industry, ASTM STP 1354,* Sabol, G. P.; Moon, G. D., Eds. ASTM International, West Conshohocken, PA, 2000, pp. 609-622.

[6] Baur, K.; Garzarolli, F.; Ruhmann, H.; Sell, H. J.; Harbottle, J.; Elmoselhi, M.; Cheng, B.; Maguire, M. "Electrochemical examinations in 350 degrees C water with respect to the mechanism of corrosion-hydrogen pickup," *12th International Symposium on Zirconium in the Nuclear Industry, ASTM STP 1354,* Sabol, G. P.; Moan, G. D., Eds. ASTM International, West Conshohocken, PA, 2000, pp. 836-852, doi: 10.1520/Stp14330s.

[7] Garzarolli, F.; Cox, B.; Rudling, P. "Optimization of Zry-2 for high burnups," *16th International Symposium on Zirconium in the Nuclear Industry, ASTM STP 1529*, ASTM International, West Conshohocken, PA, 2011, pp. 711-727.

[8] Kass, S.; Kirk, W. W. "Corrosion and hydrogen absorption properties of nickel-free Zircaloy-2 and Zircaloy-4," *ASM -- Transactions*, 55, 1, 1962, pp. 77-100.

[9] Huang, P. Y.; Mahmood, S. T.; Adamson, R. B. "Effects of thermomechanical processing on in-reactor corrosion and post-irradiation mechanical properties of Zircaloy-2," *11th International Symposium on Zirconium in the Nuclear Industry*, *ASTM STP 1295*, ASTM International, West Conshohocken, PA, 1996, pp. 726-755.

[10] Miyashita, T.; Nakae, N.; Ogata, K.; Baba, T.; Kamimura, K.; Matsumoto, T.; Kakiuchi, K. "Corrosion and hydrogen pick-up behaviors of cladding and structural components in BWR high burnup 9x9 lead use assemblies," *Proceedings of 2007 LWR Fuel Performance Conference, Top Fuel*, American Nuclear Society, 2007, pp. 401-408.

[11] Couet, A.; Motta, A. T.; De Gabory, B.; Cai, Z. "Microbeam X-ray Absorption Near-Edge Spectroscopy study of the oxidation of Fe and Nb in zirconium alloy oxide layers," *Journal of Nuclear Materials,* 452, 1-3, 2014, pp. 614-627, doi: 10.1016/j.jnucmat.2014.05.047.

[12] Ensor, B.; Motta, A. T.; Bajaj, R.; Seidensticker, J. R.; Cai, Z. "XANES analysis of iron in Zircaloy-4 oxides formed at different temperatures studied with microbeam synchrotron radiation," *Proceedings of the 2015 ANS LWR Fuel Performance Conference, Top Fuel*, American Nuclear Society, 2015, pp. 13-17.

[13] Sakamoto, K.; Une, K.; Aomi, M. "Chemical State of Alloying Elemens in Oxide Layer of Zr-based Alloys," *Proceedings of the 2010 ANS LWR Fuel Performance Conference, Top Fuel*, American Nuclear Society, 2010, pp. 101-106.

[14] Gulbransen, E. A.; Andrew, K. F. "Oxidation studies on zirconium alloys in high-pressure liquid water at 360 °C," *Journal of the Electrochemical Society,* 116, 5, 1969, pp. 659-64, doi: 10.1149/1.2412002.

[15] Couet, A.; Motta, A. T.; Comstock, R. J. "Effect of alloying elements on hydrogen pickup in zirconium alloys," *17th International Symposium on Zirconium in the Nuclear Industry, ASTM STP 1543*, ASTM International, West Conshohocken, PA, 2015, pp. 479-514, doi: 10.1520/STP154320120215.

[16] Yilmazbayhan, A.; Motta, A. T.; Comstock, R. J.; Sabol, G. P.; Barry, L.; Zhonghou, C. "Structure of zirconium alloy oxides formed in pure water studied with synchrotron radiation and optical microscopy: relation to corrosion rate," *Journal of Nuclear Materials*, 324, 1, 2004, pp. 6-22, doi: 10.1016/j.jnucmat.2003.08.038.

[17] Motta, A. T.; Da Silva, M. J. G.; Yilmazbayhan, A.; Comstock, R. J.; Cai, Z.; Lai, B. "Microstructural characterization of oxides formed on model Zr alloys using synchrotron radiation," *15th International Symposium on Zirconium in the Nuclear Industry, ASTM STP 1505*, ASTM International, West Conshohocken, PA, 2009, pp. 486-506.

[18] Frahm, R. "New method for time dependent x‐ray absorption studies," *Review of Scientific Instruments,* 60, 7, 1989, pp. 2515-2518, doi: 10.1063/1.1140716.

[19] Als-Nielsen, J.; McMorrow, D., 2011; *Elements of Modern X-ray Physics*. Wiley: London, UK, 2011.

[20] Sarangi, R. "X-ray absorption near-edge spectroscopy in bioinorganic chemistry: Application to M–O(2) systems," *Coordination chemistry reviews*, 257, 2, 2013, pp. 459-472, doi: 10.1016/j.ccr.2012.06.024.

[21] Ravel, B. "A practical introduction to multiple scattering theory," *Journal of Alloys and Compounds,* 401, 1-2, 2005, pp. 118-126, doi: 10.1016/j.jallcom.2004.04.021.

[22] Ravel, B.; Newville, M. "ATHENA, ARTEMIS, HEPHAESTUS: Data analysis for X-ray absorption spectroscopy using IFEFFIT," *Journal of synchrotron radiation,* 12, 2005, pp. 537-541, doi: 10.1107/S0909049505012719.

[23] Henke, B. L.; Gullikson, E. M.; Davies, J. C. "X-Ray Interactions: Photoabsorption, Scattering, Transmission and Reflection at E = 50-30,000 eV, Z = 1-92," *Atomic Data and Nuclear Data Tables,* 54, 2, 1993, p 349, http://dx.doi.org/10.1006/adnd.1993.1025.

[24] Ravel, B.; Scorzato, C.; Siddons, D. P.; Kelly, S. D.; Bare, S. R. "Simultaneous XAFS measurements of multiple samples," *Journal of synchrotron radiation,* 17, 3, 2010, pp. 380-385, doi: 10.1107/S0909049510006230.

[25] Castelli, R. A., Chapter 1 - The Corrosion Source. In *Nuclear Corrosion Modelling*, Butterworth-Heinemann: Boston, 2009; pp 1-31.

[26] Pecheur, D.; Lefebvre, F.; Motta, A. T.; Lemaignan, C.; Wadier, J. F. "Precipitate evolution in the Zircaloy-4 oxide layer," *Journal of Nuclear Materials,* 189, 3, 1992, pp. 318-32, doi: 10.1016/0022-3115(92)90385-X.

[27] Pecheur, D.; Lefebvre, F.; Motta, A. T.; Lemaignan, C.; Charquet, D. "Effect of irradiation on the precipitate stability in Zr alloys," *Journal of Nuclear Materials,* 205, 1993, pp. 445-451, doi: 10.1016/0022-3115(93)90108-B.

[28] De Gabory, B.; Motta, A. T.; Wang, K. "Transmission electron microscopy characterization of Zircaloy-4 and ZIRLO oxide layers," *Journal of Nuclear Materials,* 456, 2015, pp. 272-280, doi: 10.1016/j.jnucmat.2014.09.073.

[29] Hatano, Y.; Isobe, K.; Hitaka, R.; Sugisaki, M. "Role of intermetallic precipitates in hydrogen uptake of Zircaloy-2," *Journal of Nuclear Science and Technology*, 33, 12, 1996, pp. 944-9, doi: 10.3327/jnst.33.944.

[30] Pourbaix, M.; Staehle, 1973; *Lectures on electrochemical corrosion*. Springer US: New York, 1973.

[31] Couet, A.; Motta, A. T.; Comstock, R. J.; Ambard, A., Oxide electronic conductivity and hydrogen pickup fraction in zr alloys. In *2014 Annual Meeting on Transactions of the American Nuclear Society and Embedded Topical Meeting: Nuclear Fuels and Structural Materials for the Next Generation Nuclear Reactors*, American Nuclear Society: Reno, NV, 2014.

[32] Couet, A.; Motta, A. T.; Comstock, R. J. "Hydrogen pickup measurements in zirconium alloys: Relation to oxidation kinetics," *Journal of Nuclear Materials*, 451, 2014, pp. 1-13.

[33] Motta, A. T.; Yilmazbayhan, A.; Comstock, R. J.; Partezana, J.; Sabol, G. P.; Lai, B.; Cai, Z. "Microstructure and Growth Mechanism of Oxide Layers Formed on Zr Alloys Studied with Micro-Beam Synchrotron Radiation," *14th International Symposium on Zirconium in the Nuclear Industry*, *ASTM STP 1467*, Rudling, P.; Kammenzind, B., Eds. ASTM International, West Conshohocken, PA, 2005, pp. 1-26, doi: 10.1520/JAI12375.

[34] Harding, J. H. "The effect of alloying elements on Zircaloy corrosion," *Journal of Nuclear Materials*, 202, 3, 1993, pp. 216-21, doi: 10.1016/0022-3115(93)90390-K.

[35] Chang, S.; Blyholder, G.; Fernandez, J. "Iron-Oxygen Interactions in an Argon Matrix," *Inorganic Chemistry*, 20, 9, 1981, pp. 2813-2817, doi: 10.1021/ic50223a015.

[36] Xue, W.; Yin, S.; Ding, X. L.; He, S. G.; Ge, M. F. "Ground state structures of Fe(2)O(4-6)(+) clusters probed by reactions with N(2)," *J Phys Chem A*, 113, 18, 2009, pp. 5302-9, doi: 10.1021/jp810426s.

Figure Captions

FIG. 16 Hydrogen pick-up fraction of Zircaloy-2 and Zircaloy-4 components at high burn-up in the BWR environment. Figure modified from [10].

FIG. 17 Post irradiation pictures showing the appearance of irradiated, reactor-exposed, water rod samples. Nodules of oxide are present on the surface of Material 17, indicating the occurrence of nodular corrosion. Images courtesy of NFD.

FIG. 18 Example cross-sectional sample prepared for microbeam synchrotron radiation examinations from irradiated water rod materials. Sample shown in figure was prepared from Material 13. Samples were prepared and imaged at the LAMDA lab at ORNL.

FIG. 19 Experimental setup for XANES experiments at the 2-ID-D beamline. As the scan moves from the metal into the oxide, (a) zirconium fluorescence and (b) XANES spectra are acquired. Numbered points in (a) and (b) are shown in (c).

FIG. 20 Edge position of XANES spectra as defined by the first maximum of the first derivative (shown in dotted lines). (a) shows the XANES spectrum and derivative for fcc Ni and (b) shows the same for NiO.

FIG. 21 XANES spectra of standard materials used for fitting the acquired spectra. (a) Nickel XANES standards. (b) Iron XANES standards.

FIG. 22 Nickel XANES spectra acquired from standards and samples. (a) nickel XANES spectra from metallic standards and from the metal (far from the oxide/metal interface) of the analyzed samples. (b) nickel XANES spectra from oxide standards and from the bulk oxide (1 μm from the oxide/water interface) of the analyzed samples.

FIG. 23 Iron XANES spectra acquired from standards and samples. (a) iron XANES spectra from metallic standards and from the metal (far from the oxide/metal interface) of the analyzed samples. (b) iron XANES spectra from oxide standards and from the bulk oxide (1 μm from the oxide/water interface) of the analyzed samples.

FIG. 24 Plots of Ni XANES spectra as a function of distance from the oxide/metal interface. (a) Results for Archive 1. (b) Results for Material 10. (c) Results for Material 13. (d). Results for Material 17. (e) Results for Material 21. Results are all plotted to reflect the same length scale. The dotted line shows the location of the oxide/water interface for each sample.

FIG. 25 Plots of Fe XANES spectra as a function of distance from the oxide/metal interface. (a) Results for Archive 1. (b) Results for Material 10. (c) Results for Material 13. (d). Results for

Material 17. (e) Results for Material 21. Results are all plotted to reflect the same length scale. The dotted line shows the location of the oxide/water interface for each sample.

FIG. 26 Nickel XANES linear combination fitting results for various points in Material 10. (a) Fitting results 10.2 μm from the oxide/metal interface in the metal. (b) Fitting results 2.8 μm from the oxide/metal interface in the oxide layer. (c) Fitting results 19.8 μm from the oxide/metal interface in the oxide layer.

FIG. 27 Plot of metallic Ni weight fraction as a function of distance from the oxide/metal interface for each of the examined samples. (a). Shows the linear combination fitting results over the whole oxide thickness range, while (b) focuses on 15 μm around the interface.

FIG. 28 Plot of metallic Fe weight fraction as a function of distance from the oxide/metal interface for each of the examined samples. (a) shows the linear combination fitting results over the whole oxide thickness range, while (b) is an expanded view of the 15 μm near the oxide/metal interface.

FIG. 29 Relation between oxidation state of standard materials to their XANES edge position. Standards used are the ones listed in **TABLE 4**. (a) shows this this relation for nickel

standards and (b) shows the relation for iron standards. Error bars are 95% confidence limits of edge energy position.

FIG. 30 XANES edge energies of (a) nickel and (b) iron as measured using the maximum of spectrum derivative. Boxed regions show edge position ± 95% confidence intervals for standard materials.